Double-Sequence Frequency Synchronization for Wideband Millimeter-Wave Systems with Few-Bit ADCs

Dalin Zhu, Ralf Bendlin, Salam Akoum, Arunabha Ghosh, and Robert W. Heath, Jr.

***Abstract*—In this paper, we propose and evaluate a novel double-sequence low-resolution frequency synchronization method in millimeter-wave (mmWave) systems. In our system model, the base station uses analog beams to send the synchronization signal with infinite-resolution digital-to-analog converters. The user equipment employs a fully digital front end to detect the synchronization signal with low-resolution analog-to-digital converters (ADCs). The key ingredient of the proposed method is the custom designed synchronization sequence pairs, from which there exists an invertible function (a ratio metric) of the carrier frequency offset (CFO) to be estimated. We use numerical examples to show that the ratio metric is robust to the quantization distortion. To implement our proposed method in practice, we propose to optimize the double-sequence design parameters such that: (i) for each individual user, the impact of the quantization distortion on the CFO estimation accuracy is minimized, and (ii) the resulting frequency range of estimation can capture as many users' CFOs as possible. Numerical results reveal that our proposed algorithm can provide a flexible means to estimate CFO in a variety of low-resolution settings.**

I. Introduction

Due to the use of large bandwidth for high-rate data communications at millimeter-wave (mmWave) frequencies [1], the sampling rate of the corresponding analog-to-digital converters (ADCs) scales up, resulting in high power consumption and hardware complexity. Reducing ADC resolution is a solution to reduce implementation costs [2]. The use of low-precision ADCs, though, brings new design challenges to practical cellular networks. Implementing low-resolution ADCs in communications systems has been investigated in various aspects, including input signal optimization [3], [4], mutual information analysis [5]-[7], channel estimation [8], [9], uplink multiuser detection [10]-[12], and frame timing synchronization [13]. In practice, low-resolution quantization will also impair the frequency synchronization performance of mmWave systems [14].

Frequency synchronization, including both carrier frequency offset (CFO) estimation and compensation, usually happens after the frame/symbol timing position has been correctly detected [13]. As a multicarrier transmission strategy, orthogonal frequency division multiplexing (OFDM) is especially sensitive to the CFO caused by mismatches between the transmitter and receiver local oscillators and/or Doppler shifts due to a relative motion between the transmitter and receiver [15], [16]. In typical OFDM systems, the CFO can correspond to several tens of the subcarrier spacing, and can be divided into an integer component and a fractional part for the purpose of signal processing. Without frequency synchronization, the CFO may corrupt the orthogonality among the subcarriers in the OFDM system, resulting in severe inter-carrier interference (ICI) and degrading the corresponding link error rate and throughout performance [17].

Blind CFO estimation methods were developed in [18]-[22] without relying on dedicated pilots. In [18], a kurtosis-based cost function was proposed for blind CFO estimation via the forth-order statistics analysis of the received OFDM symbols. Cyclic prefix (CP) based blind CFO estimators were developed in [19], [20] by exploiting the repetitive structure of the CP samples, but their performance is subject to the frequency selectivity of the propagation channel. Multiple signal classification (MUSIC) and estimation of signal parameters via rotation invariance technique (ESPRIT) based blind CFO estimation methods were reported in [21] and [22]. These subspace based strategies, however, require a large number of samples to obtain accurate signal statistics.

There are also many pilot/sequence-aided frequency synchronization methods for OFDM systems [23]-[28]. The Cox-Schmidl algorithm [23] and variants [24]-[27] is the classic pilot-aided CFO estimation approach. In the Cox-Schmidl algorithm, a first training sequence is used to estimate the CFO with an ambiguity identical to one subcarrier spacing, while a second training sequence is employed to resolve this ambiguity. In [28], the symmetry of the Zadoff-Chu (ZC) sequences was exploited in the 3GPP long-term evolution (LTE) systems for frequency synchronization. Similar to the first training sequence in the Cox-Schmidl algorithm, the symmetry of the ZC sequences creates time-domain periodicity in one OFDM symbol duration to track the CFOs. That approach, however, only works for fractional CFO that is less than one subcarrier spacing. Of relevance in this paper, prior work [23]-[28] did not consider the impact of few-bit ADCs. Their developed synchronization pilots/sequences are therefore sensitive to the quantization distortion. This motivates us to construct new synchronization sequences that are robust to the low-resolution

Dalin Zhu is with Samsung Research America, Plano, TX, 75023 USA, e-mail: dalin.zhu@samsung.com.

Ralf Bendlin, Salam Akoum and Arunabha Ghosh are with AT&T Labs, Austin, TX, 78759 USA, e-mail: {ralf_bendlin, salam_akoum, ghosh}@labs.att.com.

Robert W. Heath, Jr. is with the Department of Electrical and Computer Engineering, The University of Texas at Austin, Austin, TX, 78712 USA, e-mail: rheath@utexas.edu.

This work was done when Dalin Zhu was with the University of Texas at Austin, and supported in part by the National Science Foundation under Grant No. ECCS-1711702, CNS-1702800 and CNS-1731658 and a gift from AT&T Labs.

quantization.

In this paper, we propose and evaluate a novel frequency synchronization method for downlink mmWave systems operating with low-resolution ADCs. The proposed strategy exhibits different frequency synchronization performances under various configurations, and can be applied in different deployment scenarios. In our system model, the base station (BS) forms directional beams in the analog domain to send the synchronization signal towards the user equipment (UE). The UE employs a fully digital front end with low-resolution ADCs to detect the synchronization signal and conduct frequency synchronization. We focus on designing new synchronization sequences that are robust to the quantization distortion. We summarize the main contributions of the paper as follows:

- *New frequency synchronization sequences design*: We develop a double-sequence high-resolution CFO estimation method for mmWave systems operating with low-resolution ADCs. In the proposed method, we custom design two sequences (i.e., a sequence pair) for frequency synchronization. They are sent by the BS across two consecutive synchronization time-slots. We refer to the sequence pair as auxiliary sequences in the proposed method. The key ingredient of the custom designed double-sequence structure is a ratio measure derived from the sequence pair, which is an invertible function of the CFO to be estimated. We use numerical examples to show that the ratio measure is robust to the quantization distortion brought by low-precision ADCs.
- *Performance analysis of proposed low-resolution frequency synchronization method*: Leveraging Bussgang's decomposition theorem [29], we derive the variance of the CFO estimate obtained via the proposed double-sequence based method operating with low-resolution (e.g., 2-4 bits) ADCs. The analytical results reveal that the CFO estimation performance highly depends on the double-sequence design parameters, which can be further optimized for various deployment scenarios.

For practical implementation of our proposed low-resolution frequency synchronization method, we first categorize all active UEs trying to simultaneously synchronize to the network as a virtual UE characterized by a set of common system-specific parameters. We then optimize the double-sequence design parameters over a set of potential values to minimize the CFO estimation error variance for the virtual UE. Note that minimizing this estimation error variance for the virtual UE can better trade off the CFO estimation accuracy and the frequency range of estimation for the actual UEs. We also implement additional signaling support and procedure at both the BS and UE sides to better support the optimization of the double-sequence design parameters.

We organize the rest of the paper as follows. In Section II, we specify the system and signal models for frequency synchronization in mmWave systems. In Section III, we present the design principle of the proposed auxiliary sequences based CFO estimation strategy; we also conduct performance analysis on our proposed method assuming few-bit ADCs. In Section IV, we address several practical issues of implementing the proposed double-sequence low-resolution frequency synchronization design in communications systems. We evaluate our proposed method in Section V assuming various channel models, quantization configurations and deployment scenarios. We draw our conclusions in Section VI.

Note that through Sections II and III, we consider a single-user setup to better formulate the synchronization signal model, explain the design principle of the proposed double-sequence structure, and conduct the performance analysis for low-resolution frequency synchronization. We also leverage the simple single-user scenario to clearly reveal the structural characteristics of the custom designed synchronization sequences and their advantages over the existing methods assuming low-resolution quantization. In Sections IV and V, we primarily focus on a multi-user scenario for practical implementation of our proposed strategy because of the broadcast nature of the initial access synchronization channel.

Notations: $\boldsymbol{A}$ ($\mathbf{A}$) is a matrix; $\boldsymbol{a}$ ($\mathbf{a}$) is a vector; a (a) is a scalar; $\mathbf{A}$, $\mathbf{a}$ and a are Fourier transforms of $\boldsymbol{A}$, $\boldsymbol{a}$ and a; $|a|$ is the magnitude of the complex number a; $(\cdot)^{\mathrm{T}}$ and $(\cdot)^*$ denote transpose and conjugate transpose; $((\cdot))_N$ represents the modulo-N operation; $\mathrm{sign}(\cdot)$ extracts the sign of a real number; $\lfloor x \rfloor$ gives the largest integer less than or equal to x; $\angle(a)$ calculates the argument of the complex number a; $[\boldsymbol{A}]_{i,:}$ is the i-th row of $\boldsymbol{A}$; $[\boldsymbol{A}]_{:,j}$ is the j-th column of $\boldsymbol{A}$; $[\boldsymbol{A}]_{i,j}$ is the (i,j)-th entry of $\boldsymbol{A}$; $[\boldsymbol{a}]_j$ represents the j-th element of $\boldsymbol{a}$; $\boldsymbol{I}_N$ is the $N \times N$ identity matrix; $\mathcal{N}_c(\boldsymbol{a}, \boldsymbol{A})$ is a complex Gaussian vector with mean $\boldsymbol{a}$ and covariance $\boldsymbol{A}$; $\Re\{\cdot\}$ and $\Im\{\cdot\}$ are used to extract the real and imaginary parts of given complex numbers; $\mathbb{E}[\cdot]$ is used to denote expectation; $\mathrm{diag}(\boldsymbol{a}^{\mathrm{T}})$ has $\{[\boldsymbol{a}]_j\}$ as its diagonal entries; and $\mathrm{diag}\{[\boldsymbol{a}]_j\}_{j=1}^{J}$ has $\{[\boldsymbol{a}]_j, j = 1, \cdots, J\}$ as its diagonal entries.

II. System Model for Frequency Synchronization in MmWave Systems

We consider a cellular system where synchronization and training data are sent periodically on directional beams, to support initial access [30], [31]. Directional transmission is important in a mmWave system because it enables favorable received signal power to overcome higher pathloss and noise floor. This approach is used in the 3GPP 5G New Radio (NR) [32] and has been applied in other Wi-Fi standards [33]. We assume that the UEs use fully digital front ends to detect the synchronization signal samples, which is realistic because there will only be a few antennas. In the following, we first present our employed system model, including the transceiver architecture, and antenna array configuration. We then develop the received synchronization signal model for our system and explain the conventional CFO estimation procedure using the ZC sequences.

A. Transceiver architecture, array configuration and synchronization signal structure

We consider a MIMO-OFDM system with N subcarriers. The BS has N_{tot} transmit antennas. The UE has M_{tot} receive antennas. We further assume that the BS has N_{RF} radio frequency (RF) chains, and the UE uses M_{RF} RF chains.

In this paper, we consider single-stream analog-only beamforming based directional synchronization at the BS (i.e., $N_{\mathrm{RF}} = 1$) and fully digital baseband processing at the UE (i.e., $M_{\mathrm{tot}} = M_{\mathrm{RF}}$).

Due to their constant amplitude and zero autocorrelation [34], ZC sequences are employed in the 3GPP LTE systems for downlink synchronization [35]. Denote the length of the employed ZC sequence by N_{ZC} and the sequence root index by i ($i \in \{0, \cdots, N_{\mathrm{ZC}} - 1\}$). For $m = 0, \cdots, N_{\mathrm{ZC}} - 1$, the sequence can be expressed as

$$s_i[m] = \exp\left(-\mathrm{j}\frac{\pi m(m+1)i}{N_{\mathrm{ZC}}}\right). \tag{1}$$

The cyclic auto-correlation of the ZC sequence results in a single Kronecker impulse at zero-lag correlation:

$$\chi[\upsilon] = \textstyle\sum_{m=0}^{N_{\mathrm{ZC}}-1} s_i[m]s_i^*[((m+\upsilon))_{N_{\mathrm{ZC}}}] = \delta[\upsilon], \quad \upsilon = 0, \cdots, N_{\mathrm{ZC}} - 1. \tag{2}$$

By exploiting (2), the UE finds the estimate of the frame timing position that exhibits the largest peak in the correlation [34]. Besides the good correlation properties, an odd-length ZC sequence is symmetric with respect to its central element, i.e.,

$$s_i[m'] = s_i[N_{\mathrm{ZC}} - 1 - m'], \;\; m' = 0, \cdots, \frac{N_{\mathrm{ZC}} - 1}{2}. \tag{3}$$

The UE can exploit this symmetry to perform the frequency synchronization, which will be elaborated in Section II-B.

Denote the frequency-domain modulated symbol on subcarrier $k = 0, \cdots, N-1$ by $\mathsf{d}[k]$. We map the ZC sequences to the central subcarriers as

$$\mathsf{d}[\lfloor (N - N_{\mathrm{ZC}} - 1)/2 \rfloor + m + 1] = \begin{cases} s_i[m], & m = 0, \cdots, N_{\mathrm{ZC}} - 1, \\ 0, & \text{otherwise}, \end{cases} \tag{4}$$

corresponding to the N_{ZC} subcarriers (out of N subcarriers) surrounding the DC-carrier. In this paper, we configure the DC-carrier as zero as in the LTE systems [35]; note that in the 3GPP 5G NR systems (Release 15) [32], no explicit DC-carrier is reserved for both the downlink and uplink.

B. Received synchronization signal model

To develop the received synchronization signal model, we assume: (i) a given UE $u \in \{1, \cdots, N_{\mathrm{UE}}\}$ in a single cell, where N_{UE} corresponds to the total number of active UEs in the cell of interest, and (ii) a given synchronization time-slot, which may be one OFDM symbol duration (T_{s}). In Section V, we simulate a more elaborate setting assuming multiple UEs and the frame structure adopted in the 3GPP LTE/NR.

The symbol vector d in (4) is transformed to the time-domain via N-point IFFTs, generating the discrete-time samples $n = 0, \cdots, N-1$ in one OFDM symbol duration as

$$d[n] = \frac{1}{\sqrt{N}} \sum_{k=0}^{N-1} \mathsf{d}[k] e^{\mathrm{j}\frac{2\pi k}{N}n}. \tag{5}$$

Before applying an $N_{\mathrm{tot}} \times 1$ wideband analog beamforming vector, a cyclic prefix (CP) is added to the symbol vector such that the length of the CP is greater than or equal to the maximum delay spread of the multi-path channels. Each sample in the symbol vector is then transmitted by a common wideband analog beamforming vector $\boldsymbol{f}$ from the BS, satisfying the power constraint $[\boldsymbol{f}\boldsymbol{f}^*]_{a,a} = \frac{1}{N_{\mathrm{tot}}}$, where $a = 1, \cdots, N_{\mathrm{tot}}$. In this paper, we assume that $\boldsymbol{f}$ is chosen from a given DFT beam codebook that results in the highest received signal strength among all other beam codewords in the codebook. The detailed beam search procedure is omitted in this paper as it is not relevant to our proposed synchronization sequences design. An example of the beam selection process can be found in [36], and the synchronization beam pattern was optimized in [13] for low-resolution frame timing synchronization.

Consider the b-th receive antenna ($b \in \{1, \cdots, M_{\mathrm{tot}}\}$) at UE u. After the timing synchronization and discarding the CP, the remaining time-domain received signal samples can be expressed as $\boldsymbol{q}_{u,b} = \left[q_{u,b}[0], \cdots, q_{u,b}[N-1]\right]^{\mathrm{T}}$. Denote the number of channel taps by L_u, the corresponding channel impulse response at tap $\ell \in \{0, \cdots, L_u - 1\}$ by $\boldsymbol{H}_u[\ell] \in \mathbb{C}^{M_{\mathrm{tot}} \times N_{\mathrm{tot}}}$, and additive white Gaussian noise by $w_{u,b}[n] \sim \mathcal{N}_c(0, \sigma_u^2)$. Denote the frequency mismatch with respect to the subcarrier spacing by ε_u. As the UE employs fully digital baseband processing, each receive antenna first quantizes the received synchronization signal with dedicated ADCs. Denote $\mathcal{Q}(\cdot)$ as the quantization function. For $n = 0, \cdots, N-1$, the time-domain received signal samples are

$$q_{u,b}[n] = \mathcal{Q}\left(e^{\mathrm{j}\frac{2\pi\varepsilon_u}{N}n} \sum_{\ell=0}^{L_u-1} [\boldsymbol{H}_u[\ell]]_{b,:}\, \boldsymbol{f} d[n-\ell] + w_{u,b}[n]\right). \tag{6}$$

Across all receive antennas, UE u selects the $\hat{b}$-th ($\hat{b} \in \{1, \cdots, M_{\mathrm{tot}}\}$) receive antenna that exhibits the highest received signal strength. By exploiting the symmetry of the employed ZC sequence and assuming perfect timing synchronization, the CFO can be estimated as

$$\hat{\varepsilon}_u = \frac{1}{\pi}\angle\left(\left[\sum_{n'=0}^{N/2-1} q_{u,\hat{b}}[n']d^*[n']\right]^* \times \left[\sum_{n''=N/2}^{N-1} q_{u,\hat{b}}[n'']d^*[n'']\right]\right). \tag{7}$$

UE u can then compensate the received signal samples with the estimated CFO as

$$\hat{q}_{u,b}[n] = e^{-\mathrm{j}\frac{2\pi\hat{\varepsilon}_u}{N}n} q_{u,b}[n]. \tag{8}$$

If $\mathcal{Q}(\cdot)$ in (6) corresponds to low-resolution quantization (e.g., 1-4 bits), the corresponding quantization distortion would damage the symmetry of the ZC sequence, leading to degraded CFO estimation performance.

III. Proposed Double-Sequence Frequency Synchronization

We propose a novel double-sequence frequency synchronization method. In this section, we explicitly explain the

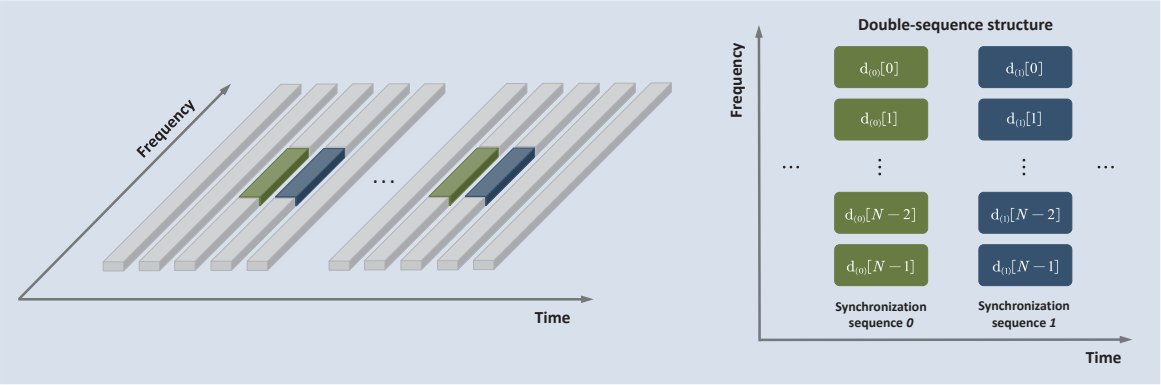

Fig. 1. Time-frequency resource mapping of the proposed double-sequence frequency synchronization. Synchronization sequences 0 and 1 in the double-sequence structure are transmitted by the BS across two consecutive synchronization time-slots.

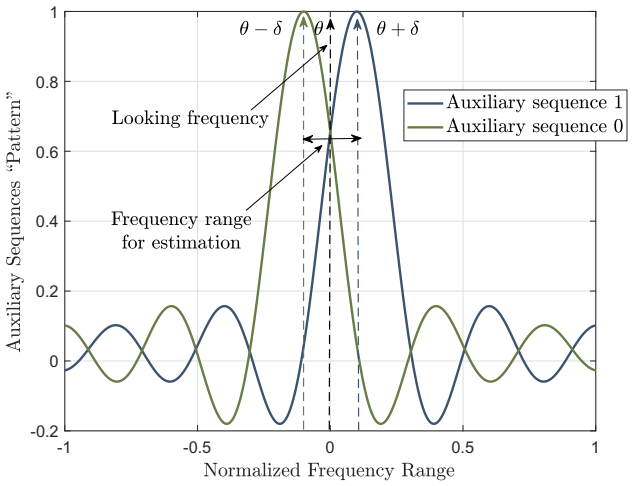

Fig. 2. Auxiliary sequences "patterns" over a given normalized frequency range. The sequence "patterns" for auxiliary sequence 0 and auxiliary sequence 1 are offset by δ to the left and right with respect to the looking frequency θ.

design principle of the proposed method assuming infinite-resolution quantization. In later sections, we will illustrate the detailed implementation procedure of our proposed method along with comprehensive performance evaluations assuming low-resolution quantization. In Fig. 1, we depict the basic double-sequence structure and its time-frequency resource mapping. As can be seen from the right-hand side of Fig. 1, two length-N sequences are periodically transmitted across two consecutive synchronization time-slots in a time-division multiplexing (TDM) manner.

A. Auxiliary sequences based double-sequence structure

We denote the time-domain samples of the two sequences by $\boldsymbol{d}_0 = \left[d_0[0], \cdots, d_0[N-1]\right]^{\mathrm{T}}$ and $\boldsymbol{d}_1 = [d_1[0], \cdots, d_1[N-1]]^{\mathrm{T}}$. Further, we construct $\boldsymbol{d}_0$ and $\boldsymbol{d}_1$ as

$$\begin{aligned}\boldsymbol{d}_0 &= [d_0[0], d_0[1], \cdots, d_0[N-1]]^{\mathrm{T}} \\ &= \left[1, e^{-\mathrm{j}(\theta-\delta)}, \cdots, e^{-\mathrm{j}(N-1)(\theta-\delta)}\right]^{\mathrm{T}} \end{aligned} \tag{9}$$

$$\begin{aligned}\boldsymbol{d}_1 &= [d_1[0], d_1[1], \cdots, d_1[N-1]]^{\mathrm{T}} \\ &= \left[1, e^{-\mathrm{j}(\theta+\delta)}, \cdots, e^{-\mathrm{j}(N-1)(\theta+\delta)}\right]^{\mathrm{T}}, \end{aligned} \tag{10}$$

and they are sent by the BS using two consecutive synchronization time-slots, say, synchronization time-slots 0 and 1. For $k = 0, \cdots, N-1$, the frequency-domain samples that correspond to $\boldsymbol{d}_0$ and $\boldsymbol{d}_1$ are

$$\begin{aligned}\mathsf{d}_0[k] &= \frac{1}{\sqrt{N}} \sum_{n=0}^{N-1} d_0[n] e^{-\mathrm{j}\frac{2\pi n}{N}k}, \\ \mathsf{d}_1[k] &= \frac{1}{\sqrt{N}} \sum_{n=0}^{N-1} d_1[n] e^{-\mathrm{j}\frac{2\pi n}{N}k}. \end{aligned} \tag{11}$$

Denote a normalized sample frequency by ν. In Fig. 2, we plot the sequence "patterns" for the two auxiliary sequences in (9) and (10), which are calculated via $\left|\sum_{n=0}^{N-1} d_0^*[n] e^{-\mathrm{j}n\nu}\right|$ and $\left|\sum_{n=0}^{N-1} d_1^*[n] e^{-\mathrm{j}n\nu}\right|$ against $\nu \in [-1, 1]$. We use the sequence "patterns" in Fig. 2 to reveal the structural characteristics and differences of the two auxiliary sequences. As can be seen from Fig. 2, the sequence "patterns" for auxiliary sequences 0 and 1 are offset by a certain value δ to the left and right with respect to the looking frequency θ. In Section IV, the auxiliary sequences design parameters θ and δ, and therefore the frequency range of estimation depicted in Fig. 2, are optimized such that many users' CFOs can be captured with promising overall frequency synchronization performance.

For synchronization time-slot 0 and $n = 0, \cdots, N-1$, we express the corresponding time-domain received signal samples as (similar to (6))

$$q_{u,b}^0[n] = \mathcal{Q}\left(e^{\mathrm{j}\frac{2\pi\varepsilon_u}{N}n} \sum_{\ell=0}^{L_u-1} [\boldsymbol{H}_u[\ell]]_{b,:}\, \boldsymbol{f}\, d_0[n-\ell] + w_{u,b}^0[n]\right). \tag{12}$$

Assuming infinite-resolution quantization and neglecting noise,

$$q_{u,b}^0[n] = e^{\mathrm{j}\frac{2\pi\varepsilon_u}{N}n} \sum_{\ell=0}^{L_u-1} [\boldsymbol{H}_u[\ell]]_{b,:}\, \boldsymbol{f}\, d_0[n-\ell]. \tag{13}$$

Defining the normalized CFO for UE u as $\mu_u = 2\pi\varepsilon_u/N$,

$$q^0_{u,b}[n] = e^{\mathrm{j}\mu_u n}\sum_{\ell=0}^{L_u-1}[\boldsymbol{H}_u[\ell]]_{b,:}\,\boldsymbol{f}d_0[n-\ell] \quad (14)$$

$$= e^{\mathrm{j}\mu_u n}\sum_{\ell=0}^{L_u-1}[\boldsymbol{H}_u[\ell]]_{b,:}\,\boldsymbol{f}e^{-\mathrm{j}(n-\ell)(\theta-\delta)} \quad (15)$$

$$= e^{\mathrm{j}\mu_u n}e^{-\mathrm{j}n(\theta-\delta)}\sum_{\ell=0}^{L_u-1}[\boldsymbol{H}_u[\ell]]_{b,:}\,\boldsymbol{f}e^{\mathrm{j}\ell(\theta-\delta)} \quad (16)$$

$$= e^{\mathrm{j}n(\mu_u-\theta+\delta)}\left[\mathbf{H}_u\left(e^{-\mathrm{j}(\theta-\delta)}\right)\right]_{b,:}\boldsymbol{f}. \quad (17)$$

Denote the selected receive antenna index by $\hat{b}$. Using the received signal samples $\boldsymbol{q}^0_{u,\hat{b}} = \left[q^0_{u,\hat{b}}[0],\cdots,q^0_{u,\hat{b}}[N-1]\right]^{\mathrm{T}}$ from synchronization time-slot 0, UE u calculates

$$p^0_{u,\hat{b}} = \left(\sum_{n=0}^{N-1}q^0_{u,\hat{b}}[n]\right)\left(\sum_{n=0}^{N-1}q^0_{u,\hat{b}}[n]\right)^* \quad (18)$$

$$= \left|\left[\mathbf{H}_u\left(e^{-\mathrm{j}(\theta-\delta)}\right)\right]_{\hat{b},:}\boldsymbol{f}\right|^2\left|\sum_{n=0}^{N-1}e^{\mathrm{j}n(\mu_u-\theta+\delta)}\right|^2 \quad (19)$$

$$\overset{(\star)}{=} \left|\left[\mathbf{H}_u\left(e^{-\mathrm{j}(\theta-\delta)}\right)\right]_{\hat{b},:}\boldsymbol{f}\right|^2\frac{\sin^2\left(\frac{N(\mu_u-\theta+\delta)}{2}\right)}{\sin^2\left(\frac{\mu_u-\theta+\delta}{2}\right)}, \quad (20)$$

where $(\star)$ is obtained via $\left|\sum_{m=1}^{M}e^{\mathrm{j}(m-1)x}\right|^2 = \frac{\sin^2\left(\frac{Mx}{2}\right)}{\sin^2\left(\frac{x}{2}\right)}$. Similarly, using the received signal samples $\boldsymbol{q}^1_{u,\hat{b}} = \left[q^1_{u,\hat{b}}[0],\cdots,q^1_{u,\hat{b}}[N-1]\right]^{\mathrm{T}}$ from synchronization time-slot 1, UE u computes

$$p^1_{u,\hat{b}} = \left(\sum_{n=0}^{N-1}q^1_{u,\hat{b}}[n]\right)\left(\sum_{n=0}^{N-1}q^1_{u,\hat{b}}[n]\right)^* \quad (21)$$

$$= \left|\left[\mathbf{H}_u\left(e^{-\mathrm{j}(\theta+\delta)}\right)\right]_{\hat{b},:}\boldsymbol{f}\right|^2\frac{\sin^2\left(\frac{N(\mu_u-\theta-\delta)}{2}\right)}{\sin^2\left(\frac{\mu_u-\theta-\delta}{2}\right)}. \quad (22)$$

By letting $\delta = 2k'\pi/N$ ($k' = 1,\cdots,\frac{N}{4}$), we can rewrite (20) and (22) as

$$p^0_{u,\hat{b}} = \left|\left[\mathbf{H}_u\left(e^{-\mathrm{j}(\theta-\delta)}\right)\right]_{\hat{b},:}\boldsymbol{f}\right|^2\frac{\sin^2\left(\frac{N(\mu_u-\theta)}{2}\right)}{\sin^2\left(\frac{\mu_u-\theta+\delta}{2}\right)},$$

$$p^1_{u,\hat{b}} = \left|\left[\mathbf{H}_u\left(e^{-\mathrm{j}(\theta+\delta)}\right)\right]_{\hat{b},:}\boldsymbol{f}\right|^2\frac{\sin^2\left(\frac{N(\mu_u-\theta)}{2}\right)}{\sin^2\left(\frac{\mu_u-\theta-\delta}{2}\right)}. \quad (23)$$

For single-path channels, i.e., $L_u = 1$, $\left|\left[\mathbf{H}_u\left(e^{-\mathrm{j}(\theta-\delta)}\right)\right]_{\hat{b},:}\boldsymbol{f}\right|^2 = \left|\left[\mathbf{H}_u\left(e^{-\mathrm{j}(\theta+\delta)}\right)\right]_{\hat{b},:}\boldsymbol{f}\right|^2$. For $L_u > 1$, if the considered mmWave channel is "sparse" in the angular domain (e.g., with very few paths having large angular spacings among them) [37], and the synchronization beam $\boldsymbol{f}$ is narrow, the resulting effective beam-space channel can therefore be approximated as

$$\sum_{\ell=0}^{L_u-1}[\boldsymbol{H}_u[\ell]]_{\hat{b},:}\,\boldsymbol{f}e^{\mathrm{j}\ell(\theta-\delta)} \approx [\boldsymbol{H}_u[\ell_{\mathrm{d}}]]_{\hat{b},:}\,\boldsymbol{f}e^{\mathrm{j}\ell_{\mathrm{d}}(\theta-\delta)} \quad (24)$$

$$\sum_{\ell=0}^{L_u-1}[\boldsymbol{H}_u[\ell]]_{\hat{b},:}\,\boldsymbol{f}e^{\mathrm{j}\ell(\theta+\delta)} \approx [\boldsymbol{H}_u[\ell_{\mathrm{d}}]]_{\hat{b},:}\,\boldsymbol{f}e^{\mathrm{j}\ell_{\mathrm{d}}(\theta+\delta)}, \quad (25)$$

where ℓ_{d} can be referred to as the index of the dominant path in the sparse channel, which is filtered out by the narrow synchronization beam $\boldsymbol{f}$ such that for $\ell \neq \ell_{\mathrm{d}}$ ($\ell = 0,\cdots,L_u-1$), $[\boldsymbol{H}_u[\ell]]_{\hat{b},:}\boldsymbol{f} \approx 0$. Under these assumptions, we can obtain $\left|\sum_{\ell=0}^{L_u-1}[\boldsymbol{H}_u[\ell]]_{\hat{b},:}\,\boldsymbol{f}e^{\mathrm{j}\ell(\theta-\delta)}\right|^2 \approx \left|\sum_{\ell=0}^{L_u-1}[\boldsymbol{H}_u[\ell]]_{\hat{b},:}\,\boldsymbol{f}e^{\mathrm{j}\ell(\theta+\delta)}\right|^2$, and therefore $\left|\left[\mathbf{H}_u(e^{\mathrm{j}(\theta-\delta)})\right]_{\hat{b},:}\boldsymbol{f}\right|^2 \approx \left|\left[\mathbf{H}_u(e^{\mathrm{j}(\theta+\delta)})\right]_{\hat{b},:}\boldsymbol{f}\right|^2$ by their definitions.

In practice, (i) the mmWave channel may not be very "sparse" in the angular domain such that the channel may comprise many paths/clusters having relatively large angular spread, and (ii) the synchronization beam $\boldsymbol{f}$ may be selected from a limited-size beam codebook having large beamwidth for each beam codeword. Under (i) and (ii), the approximations in (24) and (25) may not hold because of the multi-path/cluster interference. Note that in this paper, we do not focus on dealing with the multi-path/cluster interference, but rather the impact of low-resolution ADC quantization on the frequency synchronization performance. Hence, we simply assume that $\left|\left[\mathbf{H}_u\left(e^{-\mathrm{j}(\theta-\delta)}\right)\right]_{\hat{b},:}\boldsymbol{f}\right|^2 = \left|\left[\mathbf{H}_u\left(e^{-\mathrm{j}(\theta+\delta)}\right)\right]_{\hat{b},:}\boldsymbol{f}\right|^2$ for better illustration of the design principle, though we validate our proposed algorithm using a practical wideband channel setup with Turbo coding and mmWave specific settings in Section VI.

Using $p^0_{u,\hat{b}}$ and $p^1_{u,\hat{b}}$ in (23), UE u calculates a ratio metric as

$$\alpha_{u,\mathrm{ideal}} = \frac{p^0_{u,\hat{b}}-p^1_{u,\hat{b}}}{p^0_{u,\hat{b}}+p^1_{u,\hat{b}}} \quad (26)$$

$$= \frac{\sin^2\left(\frac{\mu_u-\theta-\delta}{2}\right)-\sin^2\left(\frac{\mu_u-\theta+\delta}{2}\right)}{\sin^2\left(\frac{\mu_u-\theta-\delta}{2}\right)+\sin^2\left(\frac{\mu_u-\theta+\delta}{2}\right)} \quad (27)$$

$$= -\frac{\sin(\mu_u-\theta)\sin(\delta)}{1-\cos(\mu_u-\theta)\cos(\delta)}, \quad (28)$$

which does not depend on the selected receive antenna index $\hat{b}$. According to [38, Lemma 1], if $|\mu_u-\theta| < \delta$, the ratio measure $\alpha_{u,\mathrm{ideal}}$ is a monotonic decreasing function of $\mu_u-\theta$ and invertible with respect to $\mu_u-\theta$. Via the inverse function, we can derive the estimated value of μ_u as

$$\hat{\mu}_u = \theta - \arcsin\left(\frac{\alpha_{u,\mathrm{ideal}}\sin(\delta)}{\sin^2(\delta)+\alpha^2_{u,\mathrm{ideal}}\cos^2(\delta)} - \frac{\alpha_{u,\mathrm{ideal}}\sqrt{1-\alpha^2_{u,\mathrm{ideal}}}\sin(\delta)\cos(\delta)}{\sin^2(\delta)+\alpha^2_{u,\mathrm{ideal}}\cos^2(\delta)}\right). \quad (29)$$

We can then obtain the super-resolution CFO estimate for UE u as $\hat{\varepsilon}_u = \frac{N}{2\pi}\hat{\mu}_u$, comprising both the integer and fractional components. Note that because $\alpha_{u,\mathrm{ideal}}$ is perfect, i.e., not impaired by noise and quantization distortion, the CFO can

$$\sigma^2_{\hat{\mu}_u,\mathrm{ax}} = \left[\frac{(1-\kappa_u)\sin^2\left(\frac{N(\mu_u-\theta+\delta)}{2}\right)\left[\sin^2\left(\frac{\mu_u-\theta-\delta}{2}\right)-\sin^2\left(\frac{\mu_u-\theta+\delta}{2}\right)\right]}{2N\left(\kappa_u+1/\gamma_{u,\mathrm{ax}}\right)\sin^2\left(\frac{\mu_u-\theta-\delta}{2}\right)\sin^2\left(\frac{\mu_u-\theta+\delta}{2}\right)}\right]^{-2} \frac{\left[1-\cos(\delta)\right]^2}{\sin^2(\delta)}\left(1+\alpha^2_{u,\mathrm{ideal}}\right), \quad (38)$$

be perfectly recovered, i.e., $\hat{\varepsilon}_u = \varepsilon_u$. As μ_u ($\hat{\mu}_u$) and ε_u ($\hat{\varepsilon}_u$) are equivalent, we use the normalized CFO μ_u and its estimate $\hat{\mu}_u$ throughout the rest of this paper unless otherwise specified. If $\mathcal{Q}(\cdot)$ in (12) corresponds to the low-resolution quantization function (e.g., 1-4 bits), the quantization distortion may damage the monotonic property of the ratio metric, resulting in increased CFO estimation errors. In Sections III-B and V, we use both analytical and numerical examples to show that our proposed design approach is robust to the low-resolution quantization.

B. Low-resolution double-sequence frequency synchronization

Assuming that the input to the quantizer is IID Gaussian, we apply Bussgang's theorem and decompose the received synchronization signal samples in (12) (i.e., synchronization time-slot 0) into two uncorrelated components, given as

$$\begin{aligned} q^0_{u,b}[n] =&(1-\kappa_u)\left(e^{\mathrm{j}\frac{2\pi\varepsilon_u}{N}n}\sum_{\ell=0}^{L_u-1}\left[\boldsymbol{H}_u[\ell]\right]_{b,:}\boldsymbol{f}d_0[n-\ell]\right. \\ &\left.+w^0_{u,b}[n]\right)+v^0_{u,b}[n] \quad (30)\\ =&(1-\kappa_u)\left(e^{\mathrm{j}n(\mu_u-\theta+\delta)}\left[\mathbf{H}_u\left(e^{-\mathrm{j}(\theta-\delta)}\right)\right]_{b,:}\boldsymbol{f}\right. \\ &\left.+w^0_{u,b}[n]\right)+v^0_{u,b}[n], \quad (31)\end{aligned}$$

where $\boldsymbol{v}^0_{u,b} = \left[v^0_{u,b}[0],\cdots,v^0_{u,b}[N-1]\right]^{\mathrm{T}}$ represents the quantization noise vector with covariance matrix $\sigma^2_{u,\mathcal{Q}}\boldsymbol{I}_N$, and

$$\sigma^2_{u,\mathcal{Q}} = \kappa_u(1-\kappa_u)\left(\mathbb{E}\left[\left|\left[\mathbf{H}_u\left(e^{-\mathrm{j}(\theta-\delta)}\right)\right]_{b,:}\boldsymbol{f}\right|^2\right]+\sigma^2_u\right). \quad (32)$$

Similarly, for auxiliary synchronization sequence 1 (synchronization time-slot 1), we express the corresponding quantized received synchronization signal samples as

$$\begin{aligned} q^1_{u,b}[n] =&(1-\kappa_u)\left(e^{\mathrm{j}n(\mu_u-\theta-\delta)}\left[\mathbf{H}_u\left(e^{-\mathrm{j}(\theta+\delta)}\right)\right]_{b,:}\boldsymbol{f}\right. \\ &\left.+w^1_{u,b}[n]\right)+v^1_{u,b}[n]. \quad (33)\end{aligned}$$

The quantization noise vector $\boldsymbol{v}^1_{u,b} = \left[v^1_{u,b}[0],\cdots,v^1_{u,b}[N-1]\right]^{\mathrm{T}}$ has covariance matrix $\sigma^2_{u,\mathcal{Q}}\boldsymbol{I}_N$. Using the received signal samples from synchronization time-slots 0 and 1 and recalling that $\hat{b}$ is the selected receive antenna index at UE u,

$$\begin{aligned} p^0_{u,\hat{b}} =& \left(\sum_{n=0}^{N-1}q^0_{u,\hat{b}}[n]\right)\left(\sum_{n=0}^{N-1}q^0_{u,\hat{b}}[n]\right)^* \quad (34)\\ =&\left[(1-\kappa_u)\left(\left[\mathbf{H}_u\left(e^{-\mathrm{j}(\theta-\delta)}\right)\right]_{\hat{b},:}\boldsymbol{f}\sum_{n=0}^{N-1}e^{\mathrm{j}n(\mu_u-\theta+\delta)}\right.\right. \\ &\left.\left.+\sum_{n=0}^{N-1}w^0_{u,\hat{b}}[n]\right)+\sum_{n=0}^{N-1}v^0_{u,\hat{b}}[n]\right] \\ &\times\left[(1-\kappa_u)\left(\left[\mathbf{H}_u\left(e^{-\mathrm{j}(\theta-\delta)}\right)\right]_{\hat{b},:}\boldsymbol{f}\sum_{n=0}^{N-1}e^{\mathrm{j}n(\mu_u-\theta+\delta)}\right.\right. \\ &\left.\left.+\sum_{n=0}^{N-1}w^0_{u,\hat{b}}[n]\right)^*+\left(\sum_{n=0}^{N-1}v^0_{u,\hat{b}}[n]\right)^*\right] \quad (35)\\ p^1_{u,\hat{b}} =& \left(\sum_{n=0}^{N-1}q^1_{u,\hat{b}}[n]\right)\left(\sum_{n=0}^{N-1}q^1_{u,\hat{b}}[n]\right)^* \quad (36)\\ =&\left[(1-\kappa_u)\left(\left[\mathbf{H}_u\left(e^{-\mathrm{j}(\theta+\delta)}\right)\right]_{\hat{b},:}\boldsymbol{f}\sum_{n=0}^{N-1}e^{\mathrm{j}n(\mu_u-\theta-\delta)}\right.\right. \\ &\left.\left.+\sum_{n=0}^{N-1}w^1_{u,\hat{b}}[n]\right)+\sum_{n=0}^{N-1}v^1_{u,\hat{b}}[n]\right] \\ &\times\left[(1-\kappa_u)\left(\left[\mathbf{H}_u\left(e^{-\mathrm{j}(\theta+\delta)}\right)\right]_{\hat{b},:}\boldsymbol{f}\sum_{n=0}^{N-1}e^{\mathrm{j}n(\mu_u-\theta-\delta)}\right.\right. \\ &\left.\left.+\sum_{n=0}^{N-1}w^1_{u,\hat{b}}[n]\right)^*+\left(\sum_{n=0}^{N-1}v^1_{u,\hat{b}}[n]\right)^*\right]. \quad (37)\end{aligned}$$

Using $p^0_{u,\hat{b}}$ in (35), $p^1_{u,\hat{b}}$ in (37) and according to (26), we can compute the corresponding ratio measure as $\alpha_u = \mathbb{E}\left[p^0_{u,\hat{b}}-p^1_{u,\hat{b}}\right]/\mathbb{E}\left[p^0_{u,\hat{b}}+p^1_{u,\hat{b}}\right]$. Note that different from $\alpha_{u,\mathrm{ideal}}$ in (26), the ratio measure α_u is no longer a strict monotonic function of the CFO to be estimated due to the noise and quantization distortions. Using $p^0_{u,\hat{b}}$ in (35), $p^1_{u,\hat{b}}$ in (37) and according to (26), we can also compute another ratio metric α'_u as $\alpha'_u = \left(p^0_{u,\hat{b}}-p^1_{u,\hat{b}}\right)/\left(p^0_{u,\hat{b}}+p^1_{u,\hat{b}}\right)$. Note that α'_u can be considered as a special case of α_u with only one sample. In the following, we leverage α_u to conduct the performance analysis. In Section V, we use α'_u to obtain the CFO estimate in all numerical examples for fair comparison with the ZC symmetry based strategy in terms of the resource overhead.

We present the following lemma to characterize the variance of the CFO estimate under low-resolution quantization.

Lemma 1. *For the proposed auxiliary synchronization sequences based low-resolution frequency synchronization, the variance of the corresponding CFO estimate is given in (38), as shown at the top of this page, where*

$$\gamma_{u,\mathrm{ax}} = \mathbb{E}\left[\left|\left[\mathbf{H}_u\left(e^{-\mathrm{j}(\theta\pm\delta)}\right)\right]_{\hat{b},:}\boldsymbol{f}\right|^2\right]/\sigma^2_u. \quad (39)$$

Proof. See Appendix. □

Note that $\left|\left[\mathbf{H}_u\left(e^{-\mathrm{j}(\theta\pm\delta)}\right)\right]_{\hat{b},:}\boldsymbol{f}\right|^2$ in (39) represents the effective beam-space channel gain, and the resulting $\gamma_{u,\mathrm{ax}}$

corresponds to the average received SNR for UE u, accounting for both the analog beamforming and the receive antenna selection effects. In later sections of our paper, we use a common system-specific SNR value to replace this user-specific received SNR to better trade off the CFO estimation accuracy and the frequency range of estimation to accommodate as many users as possible to synchronization to the network at the same time. As can be seen from (38), the CFO estimation performance of the proposed method depends on various design parameters such as the sequence length N, the quantization NMSE κ_u, the reference frequency set $\{\theta, \delta\}$, and the average received SNR $\gamma_{u,\mathrm{ax}}$.

In deriving Lemma 1, we exploit Bussgang's theorem and decompose the received synchronization signal samples into linearly uncorrelated components. Bussgang's decomposition theorem has also been extensively exploited in prior work, such as [39], [40], [41], to conduct the performance analysis for data communications in uplink MIMO systems operating with low-resolution ADCs. The main metric used in [39], [40], [41] was the signal-to-quantization-plus-noise ratio (SQNR) formulated from the decomposition as improving the spectral efficiency performance was the design target for data communications. As can be seen from (35) and (37) in the proof of Lemma 1 in the Appendix, we exploit the decomposition output differently to first compute the ratio measure, and then derive the variance of the corresponding CFO estimation errors for the auxiliary sequences based strategy. Further, the exact value of the quantization distortion is different between our proposed method and those in [39], [40], [41] because our work and prior work consider different deployment scenarios.

Analytically, it may be preferable to apply α_u at the UE to estimate the CFO because the resulted estimator is approximately unbiased (see Appendix). In practice, however, it may be difficult to execute the expectation operations in calculating α_u over a large number of samples because of the delay and overhead constraints. We can use sample means to compute the ratio metric at the UE, and in this paper, we simply use one sample, i.e., α'_u to extract the CFO estimate. It is evident that using only one sample at the UE is not optimal in terms of the unbiasedness of the estimator and the achievable estimation performance. But we use extensive numerical examples in Section V to show that using α'_u to estimate the CFO could still provide promising performance, and outperform the ZC symmetry based strategy. It is still difficult to analytically characterize the robustness of the proposed frequency synchronization method to the quantization distortion, though their closed-form CFO estimation performance is presented in (38). We therefore focus on empirical evaluations and plot the expected values of the auxiliary ratio metric $\mathbb{E}[\alpha'_u]$ in Fig. 3 for various quantization resolutions and 0 dB SNR. As shown in Fig. 3, the monotonic property does not hold for the expected ratio measure $\mathbb{E}[\alpha'_u]$ over certain frequency ranges such that directly inverting the ratio measures over these ranges may result in large estimation errors. These frequency ranges, however, are relatively small under various quantization resolutions, e.g., around $[-0.05, 0.05]$ normalized frequencies. Further, the expected ratio values computed assuming both 1-bit and 2-bit ADCs are close to those under infinite-resolution ADCs. Hence, by inverting the ratio measures obtained through few-bit ADCs, we can still expect promising CFO estimation performances for our proposed method, which are numerically verified in Section V.

As shown in (38), the CFO estimation performance of our proposed method also depends on certain double-sequence design parameter(s). Specifically, for the auxiliary sequences based strategy, these parameters correspond to the reference frequency set $\{\theta, \delta\}$. In addition to the sequence length N and the received SNR, the double-sequence design parameter(s) can be further optimized to compensate for the quantization distortion. In Section IV, we first use (38) to formulate the optimization problems; we then conclude from the corresponding solutions that in contrast to conventional pilot/sequence-aided frequency synchronization methods, our proposed strategy is capable of exploiting more design degrees of freedom to further improve the low-resolution frequency synchronization performance.

IV. Practical Implementation of Low-Resolution Frequency Synchronization

In this section, we explain the implementation procedure of our proposed double-sequence low-resolution frequency synchronization method in practical cellular networks. We focus on a multi-user scenario with various quantization configurations. We exploit the analytical performance assessment from Lemma 1 to configure the double-sequence design parameters such that for different deployment scenarios, the impact of low-resolution quantization distortion on the overall frequency synchronization performance can be minimized. In this paper, we do not provide analytical frequency synchronization performance for the multi-user setup. As will be discussed later in this section, solving the general muticast synchronization problem requires solving a complex min-max optimization problem, and our proposed grid based search algorithm does not lead to a closed-form solution. It would be of great future research interest to first derive a close-form solution to the min-max optimization problem formulated in this paper, and then conduct the analysis to better understand the overall synchronization performance for the multicast channel.

A. Basic system setup and assumption

In this paper, we consider a single cell serving multiple UEs. Note that our proposed design approach can be extended to multiple cells by scrambling the synchronization channels with different physical cell identities (PCIs) to mitigate inter-cell interference. All active UEs are equipped with fully digital front ends and low-resolution ADCs. The ADC resolutions could be different for different UEs.

The BS transmits a common synchronization signal, i.e., a synchronization signal (SS) block defined by the 3GPP, to all active UEs via directional analog beamforming. In this paper, we focus on a given synchronization beam to explain and evaluate our proposed algorithm, though the BS forms multiple analog synchronization beams in a TDM manner to transmit multiple SS blocks (an SS burst) to ensure spatial coverage (the

$$\sigma^2_{\hat{\mu}_{\rm ax}} = \left[\frac{(1-\kappa_{\rm ax})\sin^2\left(\frac{N(\mu_{\rm ax}-\theta+\delta)}{2}\right)\left[\sin^2\left(\frac{\mu_{\rm ax}-\theta-\delta}{2}\right)-\sin^2\left(\frac{\mu_{\rm ax}-\theta+\delta}{2}\right)\right]}{2N\left(\kappa_{\rm ax}+1/\gamma_{\rm ax}\right)\sin^2\left(\frac{\mu_{\rm ax}-\theta-\delta}{2}\right)\sin^2\left(\frac{\mu_{\rm ax}-\theta+\delta}{2}\right)}\right]^{-2}\frac{\left[1-\cos(\delta)\right]^2}{\sin^2(\delta)}\left(1+\alpha^2_{\rm ax}\right) \tag{41}$$

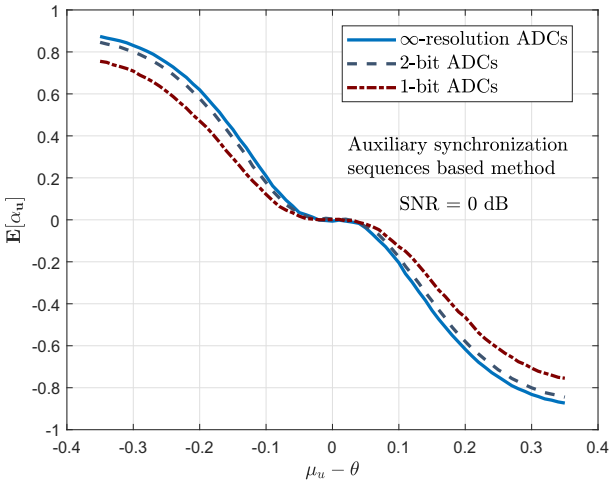

Fig. 3. Expected ratio metric value versus $\mu_u - \theta$ for the proposed auxiliary sequences based double-sequence design; 0 dB SNR is assumed with various ADC quantization resolutions.

single-stream case depicted in Fig. 4). Note that other beamforming strategies are also possible for the synchronization channel. For instance, to further reduce the synchronization delay, the multi-stream based method (shown in Fig. 4) can be used, in which multiple analog synchronization beams are simultaneously formed by the BS to transmit a given SS block. In contrast to the single-stream case, the multi-stream strategy requires a shorter SS burst to cover a given angular range, but may result in significant inter-beam interference and higher implementation complexity. Note that it may not be feasible to incorporate the digital beamforming/precoding in the synchronization channel design (e.g., in form of hybrid beamforming/precoding). This is mainly because the optimization of the digital beamforming/precoding requires explicit channel state information available at the base station, which is unrealistic during the initial access phase.

The design target here is to track all active UEs' CFOs without compromising much on each individual UE's CFO estimation performance. This can be accomplished by adjusting the frequency range of estimation of the common synchronization signal according to the distribution of all potential CFOs. In the following, we first formulate the multicast frequency synchronization problem as a min-max optimization problem assuming low-resolution quantization. By leveraging certain predefined system specific parameters, we transform the min-max problem into a minimization problem, and develop an adaptive algorithm to solve it.

B. Optimization problem formulation of proposed low-resolution frequency synchronization

To accommodate many UEs with satisfying low-resolution frequency synchronization performance, we need to incorporate the frequency range of estimation, i.e., $[\theta-\delta, \theta+\delta]$ into the optimization problem formulation. Define Θ as a set/codebook containing discrete values distributed within $[-1, 1]$. Using (38) and accounting for all $N_{\rm UE}$ active UEs, we can therefore formulate the corresponding low-resolution frequency synchronization problem as

$$\begin{aligned} \min_{\{\theta,\delta\}} \max_{\forall u} \quad & \left\{\sigma^2_{\hat{\mu}_u,{\rm ax}}\right\} \\ \text{subject to} \quad & \theta \in \Theta \\ & \delta = 2k'\pi/N, k' = 1, \cdots, \frac{N}{4} \\ & u \in \{1, \cdots, N_{\rm UE}\}, \end{aligned} \tag{40}$$

which is a min-max optimization problem and difficult to solve. To simplify (40), we first define $\kappa_{\rm ax}$, $\mu_{\rm ax}$, $\alpha_{\rm ax}$ and $\gamma_{\rm ax}$ as system specific parameters. They are predefined and can be flexibly configured by the network controller according to past measurement and system statistics. We use $\kappa_{\rm ax}$, $\mu_{\rm ax}$, $\alpha_{\rm ax}$ and $\gamma_{\rm ax}$ to replace κ_u, μ_u, $\alpha_{u,\rm ideal}$ and $\gamma_{u,\rm ax}$ in (38) and obtain 41, shown at the top of this page. We can then rewrite the optimization problem as

$$\begin{aligned} \underset{\{\theta,\delta\}}{\text{minimize}} \quad & \left\{\sigma^2_{\hat{\mu}_{\rm ax}}\right\} \\ \text{subject to} \quad & \theta \in \Theta \\ & \delta = 2k'\pi/N, k' = 1, \cdots, \frac{N}{4}. \end{aligned} \tag{42}$$

We formulate (42) by treating all active UEs as a single virtual UE with common system specific parameters $\kappa_{\rm ax}$, $\mu_{\rm ax}$, $\alpha_{\rm ax}$, $\gamma_{\rm ax}$, and a given analog synchronization beam $\boldsymbol{f}$. We need to carefully select $\kappa_{\rm ax}$, $\mu_{\rm ax}$, $\alpha_{\rm ax}$ and $\gamma_{\rm ax}$ such that $\sigma^2_{\hat{\mu}_{\rm ax}}$ for the virtual UE can represent each individual UE's error variance, i.e., $\sigma^2_{\hat{\mu}_u,{\rm ax}}$ ($u \in \{1, \cdots, N_{\rm UE}\}$), as much as possible. Note that if κ_u, μ_u, $\alpha_{u,\rm ideal}$ and $\gamma_{u,\rm ax}$ ($u \in \{1, \cdots, N_{\rm UE}\}$) vary significantly from UE to UE, the problem formulation in (41) and (42) may not be accurate. This in turn, may result in poor frequency synchronization performance in the multi-user scenario. In Section V, we use several numerical examples to characterize this aspect. Finally, we solve (42) by optimizing the double-sequence parameters such that the estimation error variance of the virtual UE is minimized.

C. Design procedure of proposed low-resolution frequency synchronization

According to (41), solving (42) requires the BS to have explicit knowledge of $\kappa_{\rm ax}$, $\mu_{\rm ax}$ ($\alpha_{\rm ax}$) and $\gamma_{\rm ax}$. Though different UEs may have different ADC resolutions, we use a

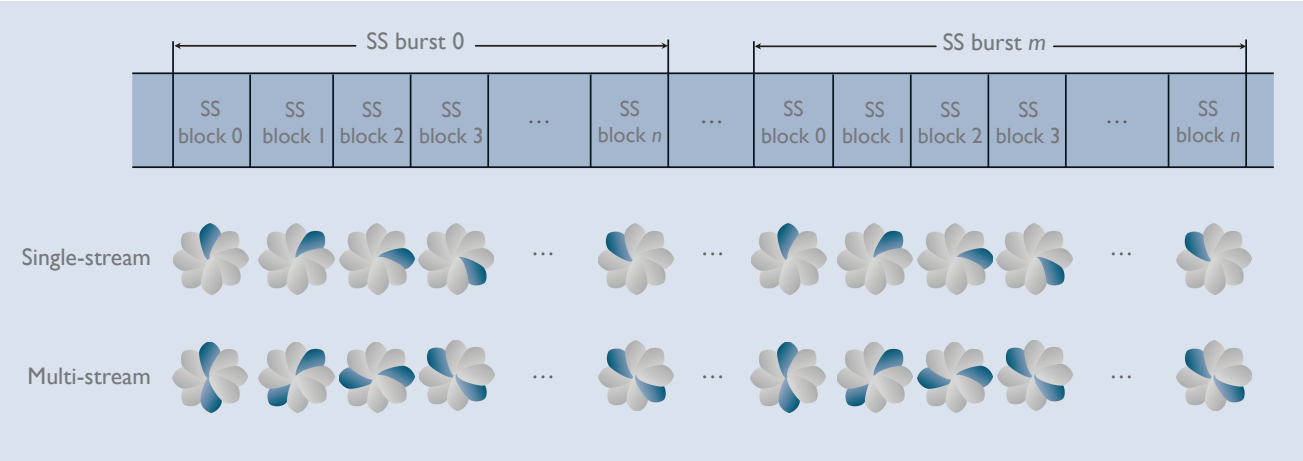

Fig. 4. Conceptual examples of various analog-only beamforming based directional synchronization strategies. One SS burst corresponds to multiple SS blocks, containing all synchronization signals and necessary control information. Multi-stream analog-only beamforming can reduce the synchronization delay relative to the single-stream case, but may also result in higher implementation complexity.

single $\kappa_{\rm ax}$ to characterize all active UEs. In Section V, we set $\kappa_{\rm ax} = 0.1175$ (i.e., 2-bit ADCs) when simulating the multi-user scenario. Further, $\gamma_{\rm ax}$ can be obtained by averaging over the received signal-to-interference-plus-noise ratios (SINRs) of all UEs. Selecting a good $\mu_{\rm ax}$ is also important for the BS to determine a proper frequency range of estimation that can capture as many UEs' CFOs as possible. In this paper, we assume that $\mu_{\rm ax} = 0$ because the normalized CFOs are usually uniformly distributed around the origin. The BS or the network controller can also configure $\mu_{\rm ax}$ using long-term system statistics such as those from previously connected UEs. For instance, for a given set of UEs whose CFOs are mainly caused by the Doppler shifts and evolved over time, it may become beneficial to exploit previously estimated CFOs, e.g., by averaging, to determine $\mu_{\rm ax}$ and track the CFOs evolution for the given UEs. In this case, the simple $\mu_{\rm ax} = 0$ setup may not be appropriate because now the normalized CFOs are not uniformly distributed around the origin. Based on these assumptions, the BS optimizes the double-sequence design parameters in (42) by conducting an exhaustive search over all potential values in the predefined codebook, e.g., Θ. In this case, the exhaustive search is a simple yet effective solution especially because the potential values of the double-sequence design parameters are well bounded by the distribution of the normalized CFOs, e.g., an uniform distribution within $(-0.1, 0.1)$.

We summarize the detailed design procedure in Algorithm 1. As can be seen from Algorithm 1, the BS needs to convey the optimized double-sequence design parameters, i.e., $\theta_{\rm opt}$ and $\delta_{\rm opt}$ to the UE so that the UE can execute the ratio metric inversion. This requires additional signaling support from the BS to the UE, which can still be implemented in the initial access process after the UE completes the symbol/frame timing synchronization and PCI detection. To reduce this signaling overhead, the BS can optimize the double-sequence design parameters in a semi-static manner, using long-term measurement and system statistics.

Further, with increase in the codebook size, the codeword search complexity of finding $\theta_{\rm opt}$ and $\delta_{\rm opt}$ would also increase. In this paper, we assume that the codeword search is conducted by the BS in a semi-static manner (e.g., in tens of seconds or even minutes) based on long-term measurement and system statistics. Even the exhaustive codeword search is performed by the BS in a more dynamic manner, the impact of the codeword search complexity on the overall implementation complexity of the proposed low-resolution frequency synchronization design is still negligible. This is

Algorithm 1 Auxiliary sequences based low-resolution frequency synchronization design

BS-SIDE PROCESSING

1 : Configuring $\kappa_{\rm ax}$, $\mu_{\rm ax}$, $\alpha_{\rm ax}$ and $\gamma_{\rm ax}$ based on long-term measurement and system statistics.
2 : Computing $\sigma^2_{\hat{\mu}_{\rm ax}}$ according to (41) and finding $\theta_{\rm opt}$ and $\delta_{\rm opt}$ that minimizes $\sigma^2_{\hat{\mu}_{\rm ax}}$ following (42) via exhaustive search over given codebooks (e.g., Θ for the looking frequency θ).
3 : If necessary, conveying the selected $\theta_{\rm opt}$ and $\delta_{\rm opt}$ to UEs after their timing synchronization.
4 : Constructing $\boldsymbol{d}_0$ and $\boldsymbol{d}_1$ according to (9) and (10), and maps their frequency-domain counterparts on given subcarriers.
5 : Probing the synchronization signal at given synchronization time-slots.

UE-SIDE PROCESSING (UE u, $u \in \{1, \cdots, N_{\rm UE}\}$)

i : Preprocessing: timing synchronization and discarding the CP.
ii : Computing the received synchronization signal strengths $p^0_{u,\hat{b}}$, $p^1_{u,\hat{b}}$ and the ratio measure $\alpha'_u = \left(p^0_{u,\hat{b}} - p^1_{u,\hat{b}}\right) / \left(p^0_{u,\hat{b}} + p^1_{u,\hat{b}}\right)$.
iii : Inverting the ratio measure α'_u following (29) to obtain the CFO estimate $\hat{\mu}_u$.
iv : Compensating the received signal samples with the estimated CFO.

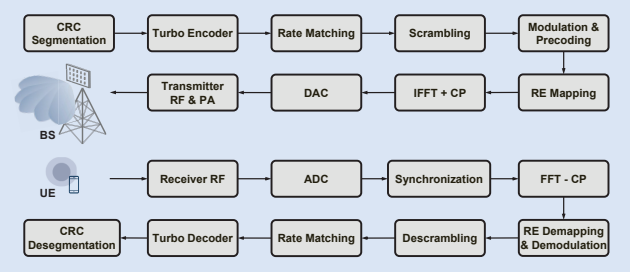

Fig. 5. Block diagram of employed link-level simulator for evaluating our proposed low-resolution frequency synchronization methods in wideband mmWave channels.

because the synchronization process (e.g., the SS burst shown in Fig. 4) is triggered by the network in a periodic manner with configurable time period between two consecutive synchronization processes (e.g., a minimum 20 ms is defined in the 3GPP 5G NR [32]). This time period is more than enough to execute the exhaustive codeword search (multiple arithmetic additions and multiplications) to find θ_{opt} and δ_{opt}. Further, the codeword search does not introduce additional implementation complexity to the UE side.

V. Numerical Results

In this section, we evaluate our proposed auxiliary sequences based frequency synchronization method assuming low-resolution (e.g., 1-4 bits) ADCs. Both the BS and UE employ a uniform linear array (ULA) with inter-element spacing $\lambda/2$, where λ represents the wavelength corresponding to the carrier frequency. Throughout the simulation section, we assume that $N_{\text{tot}} = 16$ and $M_{\text{tot}} = 8$. We consider wideband mmWave channels to evaluate our proposed algorithm, incorporating a single UE or multiple UEs. When simulating both the single-user and multi-user settings, we optimize the double-sequence design parameters to construct the corresponding synchronization sequences, though the optimization problem is formulated only for the multi-user scenario in Section IV. Optimizing the double-sequence design parameters for the single-user scenario is primarily for fair simulation comparison between our proposed method and the ZC symmetry based approach. Recall that we directly apply $\alpha'_u = \left(p^0_{u,\hat{b}} - p^1_{u,\hat{b}}\right) / \left(p^0_{u,\hat{b}} + p^1_{u,\hat{b}}\right)$ to extract the CFO estimate for fair comparison with the ZC symmetry based strategy in terms of the resource overhead, though the sequence optimization including the formulation of the optimization metric in (41) is conducted using $\alpha_u = \mathbb{E}\left[\left(p^0_{u,\hat{b}} - p^1_{u,\hat{b}}\right)\right] / \mathbb{E}\left[\left(p^0_{u,\hat{b}} + p^1_{u,\hat{b}}\right)\right]$ (see Appendix). The simulation settings of the common parameters are similar to those for the multi-user case, which have been discussed in Section IV.

A. Wideband mmWave channels with a single UE

We start by evaluating the frame error rate (FER) of our proposed method assuming few-bit ADCs. We present the block diagram of our link-level simulator in Fig. 5, which includes a complete chain of Turbo coding/decoding, OFDM and DAC/ADC modules. We assume perfect channel estimation, frame timing synchronization and infinite-resolution DACs. We adopt the 3GPP 5G tapped delay line (TDL-A) wideband channel model [42] into the link-level simulation assuming 30 GHz carrier frequency and a 80 MHz RF bandwidth. We provide other simulation assumptions such as the assumed OFDM numerology and the modulation and coding scheme (MCS) in Table I. According to these settings, a 0.1 normalized CFO corresponds to a 1.95 MHz time-domain CFO or 65 ppm of the 30 GHz carrier frequency. In Figs. 6(a) and 6(b), we plot the FER performances assuming both 2-bit and 3-bit ADCs. As can be seen from Fig. 6, our proposed auxiliary sequences based frequency synchronization strategy significantly outperforms the ZC sequence based CFO estimation method. Further, in the low-to-medium SNR regime (e.g., -10 dB $\sim$ 10 dB), our proposed method shows error rate performances close to the ideal case without CFO. For our proposed method and the ZC sequence based strategy, we

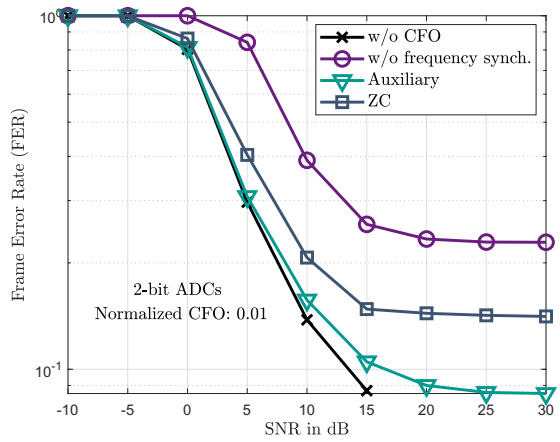

(a)

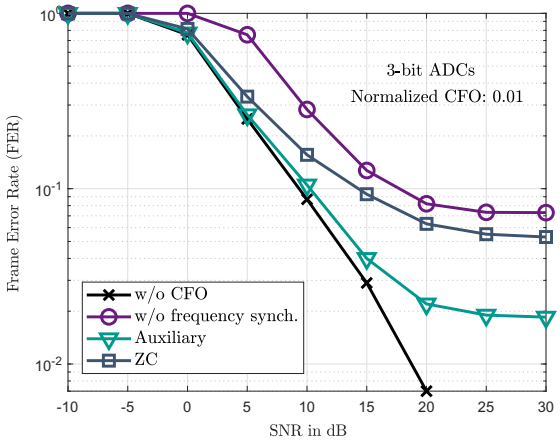

(b)

Fig. 6. Frame error rate performances of our proposed auxiliary sequences based low-resolution frequency synchronization method. The ZC sequence based method is evaluated for comparison. The perfect case without CFO and the case with CFO but without any frequency synchronization are plotted as benchmarks. The normalized CFO is set to 0.01. Other simulation assumptions are given in Table I. (a) 2-bit ADCs. (b) 3-bit ADCs.

TABLE I
SIMULATION ASSUMPTIONS AND PARAMETERS.

SYSTEM PARAMETERS	SIMULATION ASSUMPTIONS
Carrier frequency	30 GHz
System bandwidth	80 MHz
FFT size	1024
Sequence length	64 (unless otherwise specified)
Subcarrier spacing	120 KHz
OFDM symbol duration (μs)	8.33
CP length (μs)	0.82
Channel coding	Turbo
MCS	QPSK, code rate $1/2$
Channel model	3GPP 5G NR TDL-A [42]
Channel estimation	Ideal

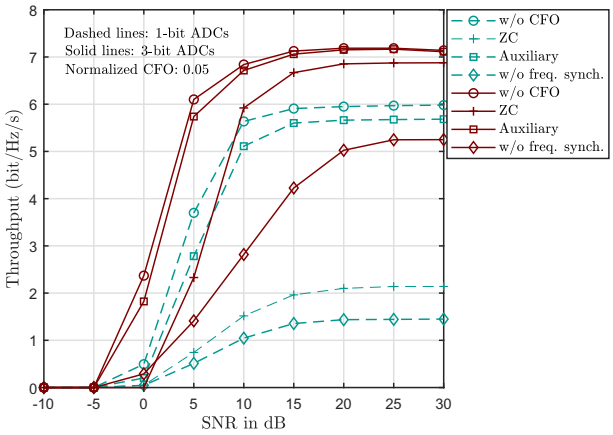

(a)

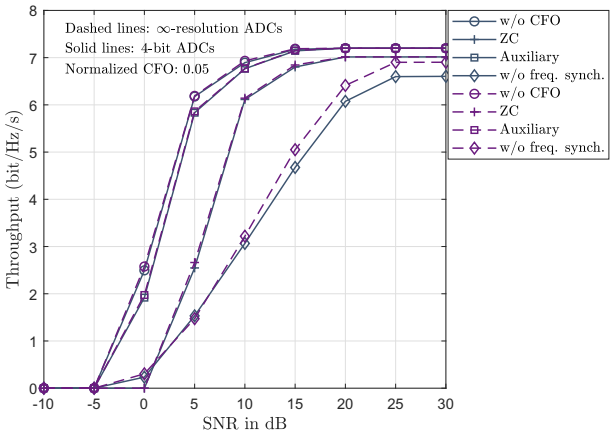

(b)

Fig. 7. Throughput performances versus SNRs of our proposed auxiliary sequences based low-resolution frequency synchronization method. The ZC sequence based method is evaluated for comparison. The perfect case without CFO and the case with CFO but without any frequency synchronization are plotted as benchmarks. The normalized CFO is set to 0.05. Other simulation assumptions are given in Table I. (a) 1-bit and 3-bit ADCs. (b) 4-bit and infinite-resolution ADCs.

can observe error floors at high SNRs.

In Fig. 7, we evaluate the throughput performances for our proposed method assuming various quantization resolutions. We compare 1-bit and 3-bit ADCs in Fig. 7(a) and observe that our proposed method outperforms the ZC sequence based strategy (similar to Fig. 6) for 0.05 normalized CFO. For instance, at 20 dB SNR, the throughput of our proposed auxiliary sequences based method is 3 bit/s/Hz higher than that of the ZC sequence based strategy assuming 1-bit ADCs. The corresponding throughput gain is 150%. With increase in the quantization resolution, this performance gap reduces. In Fig. 7(b), we examine our proposed design approach under 4-bit and infinite-resolution ADCs. The performance differences between 4-bit quantization and infinite-resolution quantization are marginal.

In Fig. 8(a), we plot the MSEs of the CFO estimates for various frequency synchronization methods. The MSE of the CFO estimate is calculated as $\mathbb{E}\left[|\varepsilon-\hat{\varepsilon}|^2\right]$, where ε is the exact CFO (without normalization) and $\hat{\varepsilon}$ is its estimated counterpart. It is evident from Fig. 8(a) that our proposed CFO estimation strategy is better than the conventional ZC sequence based approach for a wide range of frequencies. Further, the MSEs of our proposed method are almost identical across the $[-0.05, 0.05]$ frequency range of interest. This is because our proposed method can provide super-resolution CFO estimate as long as the monotonic property holds. Similar observations are obtained in Fig. 8(b), in which the FER performances are evaluated against various normalized CFOs.

In Fig. 9, we examine the impact of the overall synchronization sequence length on the low-resolution frequency synchronization performance. Here, the overall sequence length L_{seq} corresponds to $2N$ for the double-sequence structure, and N_{ZC} for the ZC symmetry based strategy. It can be seen from Fig. 9(a) that a longer overall sequence length does not necessarily result in a better CFO estimation performance for the ZC sequence based method assuming low-resolution quantization. At relatively high SNR, e.g., 20 dB in this example, the quantization distortion dominates the performance, and may severely corrupt the symmetry of the ZC sequence especially when a longer overall sequence length is assumed. With increase in L_{seq}, however, the low-resolution frequency synchronization performance improves for our proposed auxiliary sequences based method. In Fig. 9(b), we compute the resource overhead (OH) in percentile by assuming a total of $N_{\text{RE}} = 128$ resource elements available for transmitting the synchronization sequence. For instance, if $L_{\text{seq}} = 64$, the corresponding resource OH is $L_{\text{seq}}/N_{\text{RE}} = 64/128 = 50\%$. This number becomes to 100% for $L_{\text{seq}} = 128$. It is evident

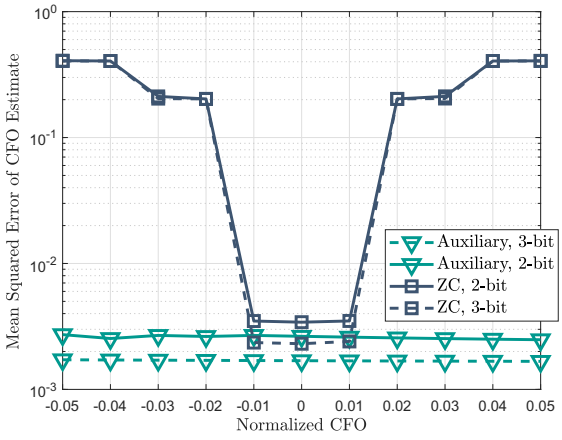

(a)

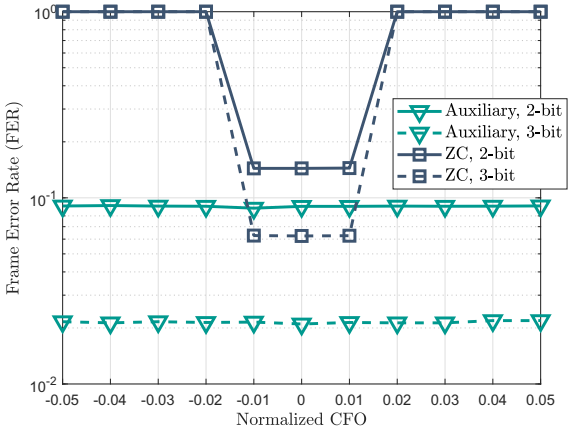

(b)

Fig. 8. Low-resolution frequency synchronization performance evaluations under various normalized CFO values. The assumed quantization resolutions for the ADCs are 2 and 3 bits with 20 dB SNR. (a) Mean squared errors of the CFO estimates obtained via the ZC sequence based method and our proposed auxiliary sequences based method. (b) Frame error rate performances of the ZC sequence based method and our proposed auxiliary sequences based method.

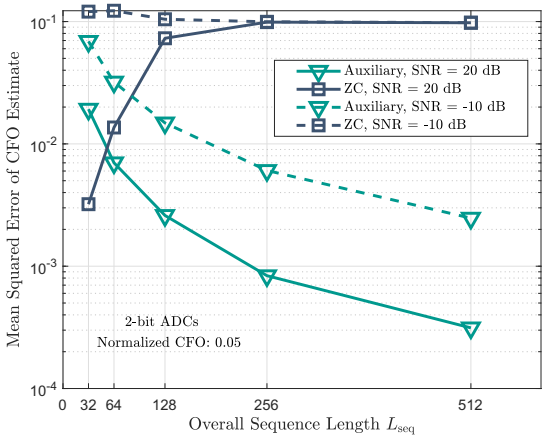

(a)

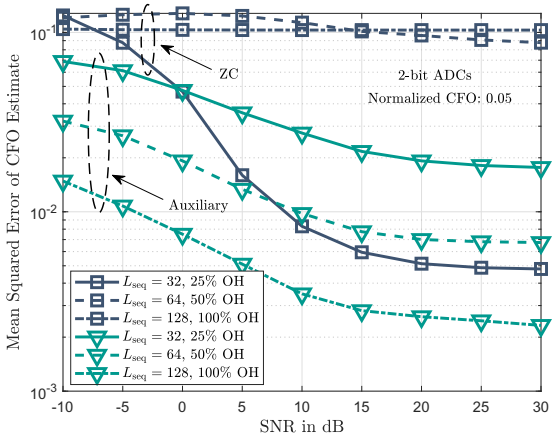

(b)

Fig. 9. Impact of the sequence length on the low-resolution CFO estimation performance for the ZC sequence based method and our proposed double-sequence based strategy. The assumed quantization resolution for the ADCs is 2 bits. (a) Mean squared errors of the CFO estimates are plotted against various sequence lengths assuming -10 dB and 20 dB SNRs. (b) Mean squared errors of the CFO estimates are plotted against various SNRs. The assumed overall sequence lengths (L_{seq}) are 32, 64 and 128, corresponding to 25%, 50% and 100% resource overheads (OHs) with a total of $N_{\text{RE}} = 128$ resource elements available for synchronization ($L_{\text{seq}}/N_{\text{RE}}$).

from Fig. 9(b) that except for $L_{\text{seq}} = 32$ (25% resource OH) at relatively high SNR, our proposed method even exhibits a better low-resolution CFO estimation performance than the ZC symmetry based strategy with a reduced resource overhead.

B. Wideband mmWave channels with multiple UEs

In this part of the simulation, we consider multiple UEs with 2-bit ADCs equipped each. Other simulation parameters and the wideband channel model are the same as those in Section V-A. We evaluate our proposed method assuming a total of 10 UEs. Their normalized CFOs are randomly distributed within the given intervals $[-0.02, 0.02]$, $[-0.03, 0.03]$, $[-0.05, 0.05]$, $[-0.07, 0.07]$ and $[-0.1, 0.1]$ (frequency ranges of normalized CFOs). Further, we focus on optimizing the double-sequence design parameters, and therefore the frequency range of estimation, to accommodate many UEs without alternating the sequence length. In the proposed auxiliary sequences based method, configuring the frequency range of estimation can be achieved by simply varying θ and δ.

In Fig. 10, we examine the impact of the frequency range of estimation on the frequency synchronization performances. It is evident from Fig. 10 that by increasing the frequency range of estimation from $[-0.01, 0.01]$ to $[-0.03, 0.03]$, the CFO estimation MSEs reduce. By further enlarging the frequency range of estimation to accommodate even more UEs (e.g., from $[-0.03, 0.03]$ to $[-0.08, 0.08]$), however, the overall CFO estimation performance degrades. These performance variations result from the fact that the frequency range of estimation ($[\theta - \delta, \theta + \delta]$ in this example) is not optimized according to the CFO distribution and the received SNRs. Finally, we plot the optimal case that uses θ_{opt} and δ_{opt} (obtained via (42)) to construct the auxiliary sequences in Fig. 10. It can be observed that the corresponding CFO estimation performance is the best

$$\alpha_u = \frac{\mathbb{E}\left[p^0_{u,\hat{b}} - p^1_{u,\hat{b}}\right]}{\mathbb{E}\left[p^0_{u,\hat{b}} + p^1_{u,\hat{b}}\right]} \tag{47}$$

$$= \frac{\left|\sum_{n=0}^{N-1} e^{\mathrm{j}n(\mu_u-\theta+\delta)}\right|^2 - \left|\sum_{n=0}^{N-1} e^{\mathrm{j}n(\mu_u-\theta-\delta)}\right|^2}{\left(\left|\sum_{n=0}^{N-1} e^{\mathrm{j}n(\mu_u-\theta+\delta)}\right|^2 + \left|\sum_{n=0}^{N-1} e^{\mathrm{j}n(\mu_u-\theta-\delta)}\right|^2\right) + 2/\gamma_{u,\mathrm{ax}} + \frac{2\kappa_u}{1-\kappa_u}\left(1+1/\gamma_{u,\mathrm{ax}}\right)}. \tag{48}$$

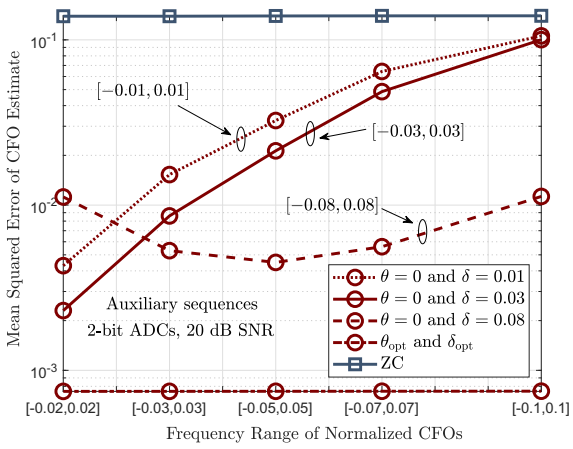

Fig. 10. Low-resolution frequency synchronization performance evaluations under various frequency ranges of normalized CFOs in a multi-user scenario. A total of 10 UEs are assumed with each of them having a 2-bit ADCs receiver. Their normalized CFOs are randomly distributed within the given frequency ranges. The SNR is 20 dB. Mean squared errors of the CFO estimates obtained via the proposed auxiliary sequences based method under various frequency ranges of estimation.

among all configurations and consistent across all frequency ranges of CFOs.

VI. Conclusions

In this paper, we custom designed a novel double-sequence structure, i.e., auxiliary sequences, for frequency synchronization in mmWave systems operating with low-resolution ADCs. We used analytical and numerical examples to show that our proposed method is robust to the low-resolution quantization for a variety of network settings. We concluded from extensive empirical results that under low-resolution ADCs: (i) our proposed strategy provides promising overall frequency synchronization performance that can better trade off the CFO estimation accuracy and the frequency range of estimation, and (ii) our custom designed auxiliary sequences outperform the ZC sequences in estimating the frequency offset.

Appendix

Proof of Lemma 1

For UE u, by denoting $\mathsf{h}^{(\theta,\delta)}_{u,\hat{b}} = \left[\mathbf{H}_u\left(e^{-\mathrm{j}(\theta-\delta)}\right)\right]_{\hat{b},:}\boldsymbol{f} = \left[\mathbf{H}_u\left(e^{-\mathrm{j}(\theta+\delta)}\right)\right]_{\hat{b},:}\boldsymbol{f}$, we can first calculate $\mathbb{E}\left[p^0_{u,\hat{b}}\right]$ as

$$\begin{aligned}\mathbb{E}\left[p^0_{u,\hat{b}}\right] &= (1-\kappa_u)^2\left|\sum_{n=0}^{N-1} e^{\mathrm{j}n(\mu_u-\theta+\delta)}\right|^2 \mathbb{E}\left[\left|\mathsf{h}^{(\theta,\delta)}_{u,\hat{b}}\right|^2\right] \\ &+ (1-\kappa_u)^2\sigma_u^2 \\ &+ \kappa_u(1-\kappa_u)\left(\mathbb{E}\left[\left|\mathsf{h}^{(\theta,\delta)}_{u,\hat{b}}\right|^2\right] + \sigma_u^2\right).\end{aligned} \tag{43}$$

Similarly,

$$\begin{aligned}\mathbb{E}\left[p^1_{u,\hat{b}}\right] &= (1-\kappa_u)^2\left|\sum_{n=0}^{N-1} e^{\mathrm{j}n(\mu_u-\theta-\delta)}\right|^2 \mathbb{E}\left[\left|\mathsf{h}^{(\theta,\delta)}_{u,\hat{b}}\right|^2\right] \\ &+ (1-\kappa_u)^2\sigma_u^2 \\ &+ \kappa_u(1-\kappa_u)\left(\mathbb{E}\left[\left|\mathsf{h}^{(\theta,\delta)}_{u,\hat{b}}\right|^2\right] + \sigma_u^2\right).\end{aligned} \tag{44}$$

Based on (43) and (44), we can then obtain

$$\begin{aligned}\mathbb{E}\left[p^0_{u,\hat{b}} - p^1_{u,\hat{b}}\right] &= (1-\kappa_u)^2\mathbb{E}\left[\left|\mathsf{h}^{(\theta,\delta)}_{u,\hat{b}}\right|^2\right] \\ &\times\left(\left|\sum_{n=0}^{N-1} e^{\mathrm{j}n(\mu_u-\theta+\delta)}\right|^2 - \left|\sum_{n=0}^{N-1} e^{\mathrm{j}n(\mu_u-\theta-\delta)}\right|^2\right)\end{aligned} \tag{45}$$

$$\begin{aligned}\mathbb{E}\left[p^0_{u,\hat{b}} + p^1_{u,\hat{b}}\right] &= (1-\kappa_u)^2\mathbb{E}\left[\left|\mathsf{h}^{(\theta,\delta)}_{u,\hat{b}}\right|^2\right] \\ &\times\left(\left|\sum_{n=0}^{N-1} e^{\mathrm{j}n(\mu_u-\theta+\delta)}\right|^2 + \left|\sum_{n=0}^{N-1} e^{\mathrm{j}n(\mu_u-\theta-\delta)}\right|^2\right) \\ &+ 2\left[(1-\kappa_u)^2\sigma_u^2 + \sigma^2_{u,\mathcal{Q}}\right].\end{aligned} \tag{46}$$

Denote by $\gamma_{u,\mathrm{ax}} = \mathbb{E}\left[\left|\mathsf{h}^{(\theta,\delta)}_{u,\hat{b}}\right|^2\right] / \sigma_u^2$. Using (45) and (46), we can express α_u as in (48), shown at the top of this page. It is evident from (48) that α_u depends on the SNR and the quantization distortion factor. Assuming high *received* SNR (high-power regime with very large N_{tot} and receive processing with antenna selection), we can approximate $1/\gamma_{u,\mathrm{ax}}$ as zero. Further, for low-resolution quantization ($2 \sim 4$ bits), we can also approximate $\kappa_u/(1-\kappa_u)$ as zero. Hence,

$$\alpha_u \approx \frac{\left|\sum_{n=0}^{N-1} e^{\mathrm{j}n(\mu_u-\theta+\delta)}\right|^2 - \left|\sum_{n=0}^{N-1} e^{\mathrm{j}n(\mu_u-\theta-\delta)}\right|^2}{\left|\sum_{n=0}^{N-1} e^{\mathrm{j}n(\mu_u-\theta+\delta)}\right|^2 + \left|\sum_{n=0}^{N-1} e^{\mathrm{j}n(\mu_u-\theta-\delta)}\right|^2} \tag{49}$$

$$\mathbb{E}\left[\breve{\mu}_u\right] = \theta - \mathbb{E}\left[\arcsin\left(\frac{\alpha_u \sin(\delta) - \alpha_u\sqrt{1-\alpha_u^2}\sin(\delta)\cos(\delta)}{\sin^2(\delta)+\alpha_u^2\cos^2(\delta)}\right)\right] \tag{52}$$

$$\approx \theta - \arcsin\left(\frac{-\sin(\mu_u-\theta)+\sin(\mu_u-\theta)\cos(\delta)\frac{\sqrt{1-\sin^2(\mu_u-\theta)\sin^2(\delta)}}{1-\cos(\mu_u-\theta)\cos(\delta)}}{\left(1-2\cos(\mu_u-\theta)\cos(\delta)+\cos^2(\delta)\right)/\left(1-\cos(\mu_u-\theta)\cos(\delta)\right)}\right) \tag{53}$$

$$= \theta - \arcsin\left(-\sin(\mu_u-\theta)\frac{1-\cos(\mu_u-\theta)\cos(\delta)-\cos(\delta)\sqrt{\left(1-\cos(\mu_u-\theta)\cos(\delta)\right)^2-\sin^2(\mu_u-\theta)\sin^2(\delta)}}{1-2\cos(\mu_u-\theta)\cos(\delta)+\cos^2(\delta)}\right) \tag{54}$$

$$= \theta - \arcsin\left(-\sin(\mu_u-\theta)\frac{1-\cos(\delta)\left(\cos(\mu_u-\theta)+\sqrt{\left(1-\cos(\mu_u-\theta)\cos(\delta)\right)^2-\sin^2(\mu_u-\theta)\sin^2(\delta)}\right)}{1-\cos(\delta)\left(\cos(\mu_u-\theta)+\cos(\mu_u-\theta)-\cos(\delta)\right)}\right) \tag{55}$$

$$= \theta - (\theta-\mu_u) \tag{56}$$

$$= \mu_u \tag{57}$$

$$= \frac{\sin^2\left(\frac{\mu_u-\theta-\delta}{2}\right)-\sin^2\left(\frac{\mu_u-\theta+\delta}{2}\right)}{\sin^2\left(\frac{\mu_u-\theta-\delta}{2}\right)+\sin^2\left(\frac{\mu_u-\theta+\delta}{2}\right)}$$

$$= -\frac{\sin(\mu_u-\theta)\sin(\delta)}{1-\cos(\mu_u-\theta)\cos(\delta)}. \tag{50}$$

In the following, we leverage the approximation in (49) to show the approximate unbiasedness of our proposed frequency estimator. Note that for moderate received SNR and 1-bit quantization, the approximation in (49) may no longer hold such that α_u may still depend on the SNR and the quantization distortion factor. In this case, our proposed estimator is not (approximately) unbiased.

Motivated by (29), we formulate the corresponding frequency estimator as

$$\breve{\mu}_u = \theta - \arcsin\left(\frac{\alpha_u \sin(\delta) - \alpha_u\sqrt{1-\alpha_u^2}\sin(\delta)\cos(\delta)}{\sin^2(\delta)+\alpha_u^2\cos^2(\delta)}\right). \tag{51}$$

We plug (50) in the calculation of $\mathbb{E}\left[\breve{\mu}_u\right]$ (shown at the top of this page). It is evident from (57) that the CFO estimator $\breve{\mu}_u$ in (51) is approximately unbiased for a fixed pair (θ, μ_u) in the high-power regime.

Define $c^0_{u,\hat{b}} = \mathbb{E}\left[p^0_{u,\hat{b}} - p^1_{u,\hat{b}}\right]$ as auxiliary channel 0 and $c^1_{u,\hat{b}} = \mathbb{E}\left[p^0_{u,\hat{b}} + p^1_{u,\hat{b}}\right]$ as auxiliary channel 1. Denote the signal power of the auxiliary channel 0 output by S^0_u. According to (45), we can obtain

$$S^0_u = \left[(1-\kappa_u)^2\mathbb{E}\left[\left|\mathsf{h}^{(\theta,\delta)}_{u,\hat{b}}\right|^2\right]\sin^2\left(\frac{N(\mu_u-\theta+\delta)}{2}\right)\right.$$
$$\left.\times\frac{\sin^2\left(\frac{\mu_u-\theta-\delta}{2}\right)-\sin^2\left(\frac{\mu_u-\theta+\delta}{2}\right)}{\sin^2\left(\frac{\mu_u-\theta+\delta}{2}\right)\sin^2\left(\frac{\mu_u-\theta-\delta}{2}\right)}\right]^2. \tag{58}$$

Denote the quantization-plus-noise power of the auxiliary channel 1 output for UE u by N^1_u. According to (46), we have

$$N^1_u = 4\left[\left(1-\kappa_u\right)^2\sigma_u^2+\sigma^2_{u,\mathcal{Q}}\right]^2 \tag{59}$$

$$= 4\left[(1-\kappa_u)\left(\kappa_u\mathbb{E}\left[\left|\mathsf{h}^{(\theta,\delta)}_{u,\hat{b}}\right|^2\right]+\sigma_u^2\right)\right]^2. \tag{60}$$

The variance of the CFO estimate can then be expressed as [43, equation 3.26]

$$\sigma^2_{\hat{\mu}_u,\mathrm{ax}} = \frac{1}{\varsigma^2_{\mathrm{ax}}S^0_u/N^1_u}\left[1+\mathcal{M}^2_{\mathrm{ax}}(\mu_u)\right], \tag{61}$$

where $\mathcal{M}_{\mathrm{ax}}(\mu_u) = \alpha_{u,\mathrm{ideal}}$ for the proposed auxiliary sequences based method, and ς_{ax} represents the slope of $\mathcal{M}_{\mathrm{ax}}(\cdot)$ at θ, i.e.,

$$\varsigma_{\mathrm{ax}} = \mathcal{M}'_{\mathrm{ax}}(\theta) = \frac{\sin(\delta)}{\cos(\delta)-1}. \tag{62}$$

By plugging (58), (60) and (62) into (61), we can obtain (38), which completes the proof.

REFERENCES

[1] R. W. Heath Jr., N. Gonzalez-Prelcic, S. Rangan, W. Roh, and A. Sayeed, "An overview of signal processing techniques for millimeter wave MIMO systems," *IEEE J. Sel. Top. Signal Process.*, vol. 10, no. 3, pp. 436–453, Feb. 2016.

[2] A. Alkhateeb, J. Mo, N. G. Prelcic, and R. W. Heath Jr., "MIMO precoding and combining solutions for millimeter-wave systems," *IEEE Commun. Mag.*, vol. 52, no. 12, pp. 122–131, Dec. 2014.

[3] A. Mezghani and J. A. Nossek, "Analysis of Rayleigh-fading channels with 1-bit quantized output," in *IEEE Intern. Symp. on Info. Theory*, Jul. 2008.

[4] J. Singh, O. Dabeer, and U. Madhow, "On the limits of communications with low-precision analog-to-digital conversion at the receiver," *IEEE Trans. Commun.*, vol. 57, no. 12, pp. 3629–2639, Dec. 2009.

[5] J. Mo and R. W. Heath Jr., "Capacity analysis of one-bit quantized MIMO systems with transmitter channel state information," *IEEE Trans. Signal Process.*, vol. 63, no. 20, pp. 5498–5512, Oct. 2015.

[6] M. T. Ivrlac and J. A. Nossek, "Challenges in coding for quantized MIMO systems," in *IEEE Intern. Symp. on Info. Theory*, Jul. 2006.

[7] B. M. Murray and I. B. Collings, "AGC and quantization effects in a zero-forcing MIMO wireless system," in *IEEE Veh. Tech. Conf.*, May 2006.

[8] T. Lok and V.-W. Wei, "Channel estimation with quantized observations," in *IEEE Intern. Symp. on Info. Theory*, Aug. 1998.

[9] G. Zeitler, G. Kramer, and A. Singer, "Bayesian parameter estimation using single-bit dithered quantization," *IEEE Trans. Signal Process.*, vol. 60, no. 6, pp. 2713–2726, Jun. 2012.

[10] S. Wang, Y. Li, and J. Wang, "Multiuser detection for uplink large-scale MIMO under one-bit quantization," in *IEEE Intern. Conf. Commun.*, Jun. 2014.

[11] J. Choi, J. Mo, and R. W. Heath Jr., "Near maximum-likelihood detector and channel estimator for uplink multiuser massive MIMO systems with one-bit ADCs," *IEEE Trans. Commun.*, vol. 64, no. 5, pp. 2005–2018, May 2016.

[12] C. Mollen, J. Choi, E. G. Larsson, and R. W. Heath Jr., "Uplink performance of wideband massive MIMO with one-bit ADCs," *IEEE Trans. Wireless Commun.*, vol. 16, no. 1, pp. 87–100, Jan. 2017.

[13] D. Zhu, R. Bendlin, S. Akoum, A. Ghosh, and R. W. Heath Jr., "Directional frame timing synchronization in wideband millimeter-wave systems with low-resolution ADCs," *arXiv preprint arXiv:1809.02890*, Aug. 2018.

[14] A. Wadhwa and U. Madhow, "Blind phase/frequency synchronization with low-precision ADC: a Bayesian approach," in *IEEE Allerton Conf. on Communication, Control, and Computing*, Oct. 2013.

[15] L. Wei and C. Schlegel, "Synchronization requirements for multi-user OFDM on satellite mobile and two-path Rayleigh fading channels," *IEEE Trans. Commun.*, vol. 43, no. 4, pp. 887–895, Apr. 1995.

[16] T. Pollet, M. Van Bladel, and M. Moeneclaey, "BER sensitivity of OFDM systems to carrier frequency offset and Wiener phase noise," *IEEE Trans. Commun.*, vol. 43, no. 4, pp. 191–193, Apr. 1995.

[17] R. Van Nee and R. Prasad, *OFDM for wireless multimedia communications*, Artech House, Inc., 2000.

[18] Y. Yao and G. B. Giannakis, "Blind carrier frequency offset estimation in SISO, MIMO, and multiuser OFDM systems," *IEEE Trans. Commun.*, vol. 53, no. 1, pp. 173–183, Jan. 2005.

[19] J.-J. van de Beek, M. Sandell, and P. O. Borjesson, "ML estimation of time and frequency offset in OFDM systems," *IEEE Trans. Signal Process.*, vol. 45, no. 7, pp. 1800–1805, Jul. 1997.

[20] Q. Cheng, "Residue carrier frequency offset estimation using cyclic prefix in OFDM systems," in *IEEE Region 10 Conf. (TENCON)*, Jan. 2009, pp. 1–5.

[21] H. Liu and U. Tureli, "A high-efficiency carrier estimator for OFDM communications," *IEEE Commun. Lett.*, vol. 2, no. 4, pp. 104–106, Apr. 1998.

[22] U. Tureli, H. Liu, and M. D. Zoltowski, "OFDM blind carrier offset estimation: ESPRIT," *IEEE Trans. Commun.*, vol. 48, no. 9, pp. 1459–1461, Sep. 2000.

[23] T. M. Schmidl and D. C. Cox, "Robust frequency and timing synchronization for OFDM," *IEEE Trans. Commun.*, vol. 45, no. 12, pp. 1613–1621, Dec. 1997.

[24] H. Minn, V. K. Bhargava, and K. B. Letaief, "A robust timing and frequency synchronization for OFDM systems," *IEEE Trans. Wireless Commun.*, vol. 2, no. 4, pp. 822–839, Jul. 2003.

[25] Z. Zhang, W. Jiang, H. Zhou, Y. Liu, and J. Gao, "High accuracy frequency offset correction with adjustable acquisition range in OFDM systems," *IEEE Trans. Wireless Commun.*, vol. 4, no. 1, pp. 228–237, Jan. 2005.

[26] M. Ghogho, P. Ciblat, A. Swami, and P. Bianchi, "Training design for repetitive-slot-based CFO estimation in OFDM," *IEEE Trans. Signal Process.*, vol. 57, no. 12, pp. 4958–4964, Dec. 2009.

[27] M. Morelli and M. Moretti, "Carrier frequency offset estimation for OFDM direct-conversion receivers," *IEEE Trans. Wireless Commun.*, vol. 11, no. 7, pp. 2670–2679, Jul. 2012.

[28] Y. Tsai and G. Zhang, "Time and frequency synchronization for 3GPP long term evolution systems," in *IEEE Veh. Tech. Conf.*, Apr. 2007, pp. 1727–1731.

[29] J. J. Bussgang, "Crosscorrelation functions of amplitude-distorted Gaussian signals," 1952.

[30] T. A. Thomas, F. W. Vook, R. Ratasuk, and A. Ghosh, "Broadcast control strategies for mmWave massive MIMO leveraging orthogonal basis functions," in *IEEE Global Telecomm. Conf.*, Dec. 2015.

[31] M. Giordani, M. Polese, A. Roy, D. Castor, and M. Zorzi, "A tutorial on beam management for 3GPP NR at mmWave frequencies," *arXiv preprint arXiv:1804.01908*, Apr. 2018.

[32] "NR; Physical Channels and Modulation," 3GPP TS 38.211, Jun. 2018. [Online]. Available: http://www.3gpp.org/ftp//Specs/archive/38_series/38.211/.

[33] P. Zhou, K. Cheng, X. Han, X. Fang, Y. Fang, R. He, Y. Long, and Y. Liu, "IEEE 802.11ay-based mmWave WLANs: design challenges and solutions," *IEEE Communications Surveys & Tutorials*, vol. 20, no. 3, pp. 1654–1681, Mar. 2018.

[34] B. M. Popovic, "Generalized chirp-like polyphase sequences with optimum correlation properties," *IEEE Trans. Inf. Theory*, vol. 38, no. 4, pp. 1406–1409, Jul. 1992.

[35] "Technical Specification Group RAN: Evolved Universal Terrestrial Radio Access (E-UTRA); Physical Channels and Modulation," 3GPP TS 36.211, Dec. 2011. [Online]. Available: http://www.3gpp.org/ftp/Specs/html-info/36211.htm.

[36] D. Zhu, J. Choi, and R. W. Heath Jr., "Auxiliary beam pair design in mmWave cellular systems with hybrid precoding and limited feedback," in *IEEE Int. Conf. Acoust. Speech Signal Process.*, Mar. 2016, pp. 3391–3395.

[37] M. Akdeniz, Y. Liu, M. Samimi, S. Sun, S. Rangan, T. S. Rappaport, and E. Erkip, "Millimeter wave channel modeling and cellular capacity evaluation," *IEEE J. Sel. Areas Commun.*, vol. 32, no. 6, pp. 1164–1179, Jun. 2014.

[38] D. Zhu, J. Choi, and R. W. Heath Jr., "Auxiliary beam pair enabled AoD and AoA estimation in closed-loop large-scale mmWave MIMO system," *IEEE Trans. Wireless Commun.*, vol. 16, no. 7, pp. 4770–4785, Jul. 2017.

[39] C. Mollen, J. Choi, E. G. Larsson, and R. W. Heath Jr., "Uplink performance of wideband massive MIMO with one-bit ADCs," *IEEE Trans. Wireless Commun.*, vol. 16, no. 1, pp. 87–100, Jan. 2017.

[40] J. Zhang, L. Dai, S. Sun, and Z. Wang, "On the spectral efficiency of massive MIMO systems with low-resolution ADCs," *IEEE Commun. Lett.*, vol. 20, no. 5, pp. 842–845, May 2016.

[41] S. Jacobsson, G. Durisi, M. Coldrey, U. Gustavsson, and C. Stubber, "Throughput analysis of massive MIMO uplink with low-resolution ADCs," *IEEE Trans. Wireless Commun.*, vol. 16, no. 6, pp. 4038–4051, Jun. 2017.

[42] "Study on channel model for frequency sepctrum above 6 GHz," 3GPP TR 38.900, Jun. 2018. [Online]. Available: http://www.3gpp.org/ftp//Specs/archive/38_series/38.900/.

[43] Y. Seliktar, "Space-time adaptive monopulse processing," *Ph.D. dissertation, Dept. Elect. Eng., Georgia Inst. of Tech., Atlanta, GA,*, Dec. 1998.

Dalin Zhu received the B.Eng. in Information Engineering from Beijing University of Posts and Telecommunications (BUPT) and M.Sc. in Electrical and Computer Engineering from Kansas State University in 2007 and 2009, respectively. He obtained his Ph.D. degree in wireless communication and networking from The University of Texas at Austin in 2019. He is now a research staff engineer with Samsung Research America.

From 2010 to 2014, he worked as a research staff member and project manager in the Dept. of Wireless Communications at NEC Laboratories China (NLC) focusing on 3GPP LTE/LTE-A standardization, TD-LTE system-level simulator development and C-RAN prototyping. From 2012 to 2013, he was a visiting scientist at the Wireless Systems Laboratory (WSL), Stanford University. From 2014 to 2015, he worked at Samsung R&D Institute China - Beijing (SRC-B) as a staff engineer working towards 5G related topics including new waveform design, massive MIMO, non-orthogonal multiple access schemes, and mmWave communications. During the summers of 2018, 2017 and 2016, he worked as an intern at AT&T Labs, Austin, TX and Huawei Technologies, Rolling Meadows, IL focusing on 5G new radio simulation and research.

Dr. Zhu was the recipient of the University Graduate Continuing Fellowship (2018-2019), Cullen M. Crain Endowed Scholarship in Engineering (2017-2018) from the University of Texas at Austin, Award of Excellence (2015/Q1) from Samsung R&D Institute China - Beijing, best paper award from Chinacom 2013 (Green Communications Symposium), and Dean's Special Award of Merit (2010-2011) from NEC Laboratories China.

Ralf Bendlin (S'07 - M'11) is a Principal Member of Technical Staff at AT&T Labs in Austin, Texas. Before joining AT&T Labs, he was a Senior Wireless Systems Architect with Intel Corporation in Portland, Oregon and a Systems Engineer with Texas Instruments Inc. in Dallas, Texas. He has worked on algorithm development, performance prediction, optimization, systems architecture, and technology strategy for current and next-generation wireless networks and has actively participated in the definition of several global communications standards for which he holds several patents.

Dr. Bendlin earned a Bachelor's degree and a Master's degree from the Munich University of Technology in Munich, Germany as well as a Master's degree and a Ph.D. from the University of Notre Dame in South Bend, Indiana. All degrees are in Electrical Engineering and Information Technology. He is a member of the Industry Advisory Council of the Department of Electrical Engineering at the University of Notre Dame and the Technical Program Chair of the IEEE GLOBECOM 2019 Workshop on High-Dimensional, Low-Resolution Architectures for Power-Efficient Wireless Communications. He has previously served as the Technical Program Chair of the 2017 IEEE International Symposium on Dynamic Spectrum Access Networks, as Guest Editor of the IEEE Transactions on Cognitive Communications and Networking (TCCN), and as a member of the Advisory Council of the College of Engineering at the University of Notre Dame.

Salam Akoum (S'07 - M'13) is a principal member of technical staff at AT&T labs, advanced radio technology group. She is an active contributor to 3GPP 5G standardization, responsible for specifications of the physical layer of the radio interface. Salam works on algorithm development and system architecture and optimization for current and next-generation wireless networks. Prior to joining AT&T labs, Salam worked at the center for Social Innovation at Hitachi America R&D, where she investigated connectivity solutions, analytics and traffic optimization for IT and OT convergence and received the Hitachi above and beyond award in 2014.

Dr. Akoum earned her Ph.D. in Electrical Engineering from the University of Texas at Austin in 2012. She graduated with a Bachelor of Engineering in Computer and Communications Engineering and a minor in Mathematics (Honors) from the American University of Beirut, Lebanon in 2006, and completed her Master of Science in Electrical Engineering from the University of Utah in 2008. She was a visiting researcher at SUPELEC, France in 2011.

Arun Ghosh received his PhD from University Illinois at Urbana-Champaign (98) and his masters and bachelors from Indian Institute of Technology Kanpur (92). He is currently the Director of Advanced Wireless Technology Group at AT&T Labs, where he is responsible for the research and development of advanced wireless technology for 5G and beyond 5G Wireless Networks. Currently he is involved in the development of many new technology concepts for beyond 5G mobile networks as they relate to mmWave communication systems, massive MIMO systems, mobile multi-hop network, low resolution ultra-massive MIMO systems, network coding etc. He is also widely recognized as the key innovator behind many revolutionary new concepts for 5G such as IAB (integrated access and backhaul), Asynchronous Multi-Point Transmission, Spatial Compression for 5G Fronthaul. His main area of research relates signal processing and communication theory but he has also worked extensively on other topics such as cloud RAN, advanced system architecture and has published extensively in these area and is a key contributor to AT&T patent portfolio on this subject. Dr. Ghosh is the recipient of the AT&T Fellow Award and has also authored several bestselling books on LTE and WiMAX.

Robert W. Heath Jr. (S'96 - M'01 - SM'06 - F'11) received the B.S. and M.S. degrees from the University of Virginia, Charlottesville, VA, in 1996 and 1997 respectively, and the Ph.D. from Stanford University, Stanford, CA, in 2002, all in electrical engineering. From 1998 to 2001, he was a Senior Member of the Technical Staff then a Senior Consultant at Iospan Wireless Inc, San Jose, CA where he worked on the design and implementation of the physical and link layers of the first commercial MIMO-OFDM communication system. Since January 2002, he has been with the Department of Electrical and Computer Engineering at The University of Texas at Austin where he is a Cullen Trust for Higher Education Endowed Professor, and is a Member of the Wireless Networking and Communications Group. He is also President and CEO of MIMO Wireless Inc. He authored "Introduction to Wireless Digital Communication" (Prentice Hall, 2017) and "Digital Wireless Communication: Physical Layer Exploration Lab Using the NI USRP" (National Technology and Science Press, 2012), and co-authored "Millimeter Wave Wireless Communications" (Prentice Hall, 2014).

Dr. Heath has been a co-author of sixteen award winning conference and journal papers including the 2010 and 2013 EURASIP Journal on Wireless Communications and Networking best paper awards, the 2012 Signal Processing Magazine best paper award, a 2013 Signal Processing Society best paper award, 2014 EURASIP Journal on Advances in Signal Processing best paper award, the 2014 Journal of Communications and Networks best paper award, the 2016 IEEE Communications Society Fred W. Ellersick Prize, the 2016 IEEE Communications and Information Theory Societies Joint Paper Award, and the 2017 Marconi Prize Paper Award. He received the 2017 EURASIP Technical Achievement award. He was a distinguished lecturer in the IEEE Signal Processing Society and is an ISI Highly Cited Researcher. In 2017, he was selected as a Fellow of the National Academy of Inventors. He is also an elected member of the Board of Governors for the IEEE Signal Processing Society, a licensed Amateur Radio Operator, a Private Pilot, a registered Professional Engineer in Texas.